Frontiers in Bioscience Landmark

Front. Biosci. (Landmark Ed) **2026**; 31(1): 47541
https://doi.org/10.31083/FBL47541

Original Research

FUBP3-Mediated Recruitment of STAT3 Complex Formation to Activate EMT Factor Twist1 and Promote Lung Cancer Metastasis

Wenying Wang[1,2,*], Liang Zhang[1], Ping Wang[1,*]

[1]Department of Radiation Oncology, Tianjin Medical University Cancer Institute & Hospital, National Clinical Research Center for Cancer, Key Laboratory of Cancer Prevention and Therapy, Tianjin's Clinical Research Center for Cancer, Tianjin Medical University, 300060 Tianjin, China
[2]Department of Radiation Oncology, Liaocheng People's Hospital, 252000 Liaocheng, Shandong, China
*Correspondence: wwying0608@tmu.edu.cn (Wenying Wang); wangping@tjmuch.com (Ping Wang)

Academic Editor: Esteban C. Gabazza
Submitted: 21 October 2025 Revised: 10 December 2025 Accepted: 19 December 2025 Published: 20 January 2026

Abstract

Background: Lung cancer is the leading cause of cancer-related mortality worldwide, and metastasis is the key factor leading to patient death. Epithelial–mesenchymal transition (EMT), which is crucial to tumor metastasis, is primarily regulated by EMT transcription factors, such as Twist1. As an RNA-binding protein, far upstream element binding protein 3 (FUBP3) shows aberrant expression in various tumors; however, its mechanistic role in lung cancer metastasis remains unclear. This study aims to elucidate the functional role of FUBP3 in lung cancer metastasis and its molecular mechanism in the regulation of Twist1. **Methods**: Bioinformatics analysis was conducted to examine FUBP3 expression patterns in lung cancer and its association with patient prognosis. The Cancer Genome Atlas database was used, and FUBP3 protein expression levels were detected in clinical lung cancer tissues by immunohistochemical analysis. Lung cancer cell lines with FUBP3 knockdown were established, and the effects of FUBP3 on the metastatic capacity of lung cancer were assessed using Transwell migration and invasion assays, 3D spheroid invasion experiments, and tail vein injection metastasis models. Changes in the expression levels of EMT markers were detected by western blot, quantitative real-time polymerase chain reaction, and immunofluorescence. The interaction between FUBP3 and signal transducer and activator of transcription 3 (STAT3) was verified by co-immunoprecipitation (Co-IP), proximity ligation assay, and immunofluorescence co-localization. The effects of STAT3 inhibitor S3I-201 on FUBP3-mediated pro-metastatic functions were assessed. **Results**: Bioinformatics analysis revealed high FUBP3 expression in lung cancer tissues, which correlated with poor patient prognosis. Notably, patients with distant metastasis (M1) stage exhibited higher FUBP3 expression than those at the no distant metastasis (M0) stage. Functional experiments confirmed that FUBP3 silencing inhibited the migration and invasion of lung cancer cells, as well as the formation of pulmonary metastatic foci *in vivo*. The knockdown of FUBP3 led to an increase in the expression of the epithelial marker E-cadherin and downregulated the expression of the mesenchymal marker vimentin, indicating that FUBP3 promotes lung cancer metastasis by promoting EMT. Subsequent analysis indicated that FUBP3 facilitates lung cancer progression by upregulating Twist1 expression. Both exhibit positive correlations in lung cancer patient tissues. Co-IP and immunofluorescence assays demonstrated a direct interaction between FUBP3 and STAT3 proteins. STAT3 silencing counteracted pro-metastatic effects associated with FUBP3 overexpression in lung cancer metastasis. Treatment with S3I-201 effectively reversed the pro-metastatic phenotype in cells with high FUBP3 expression, restored the typical patterns of EMT marker expression, and reduced the formation of metastatic foci in the *in vivo* metastasis model. **Conclusion**: This study reveals the critical role of FUBP3 in lung cancer metastasis and identifies a new regulatory axis involving FUBP3–STAT3–Twist1. FUBP3 interacts with STAT3, enhancing STAT3-dependent Twist1 expression, which promotes EMT and metastasis. FUBP3 functions as a prognostic biomarker, and STAT3 inhibitors present therapeutic strategies for lung cancer, offering novel insights for precision treatment.

Keywords: FUBP3; lung cancer; metastasis; epithelial–mesenchymal transition; Twist1

1. Introduction

Epithelial–mesenchymal transition (EMT) is a crucial process enabling tumors to gain invasive and metastatic properties [1,2]. This process allows epithelial-derived tumor cells to detach from intercellular connections and gain motility akin to mesenchymal cells, facilitating tumor metastasis [3]. EMT is primarily regulated by EMT transcription factors (EMT-TFs), including members of the snail family transcriptional repressor (SNAIL), zinc finger E-box-binding homeobox (ZEB), and twist family bHLH transcription factor (TWIST) families [1,4]. Twist1, which is a basic helix–loop–helix transcription factor, is pivotal in the EMT of various malignant tumors [5,6]. Twist1 suppresses the expression of epithelial marker genes, such as E-cadherin, by binding to Enhancer box (E-box) sequences in the promoters of target genes, while concurrently activating the transcription of mesenchymal marker genes, such as vimentin [7]. Clinical studies indicate that Twist1 is overexpressed in lung cancer, and its expression level is closely associated with tumor grading, metastasis, and patient prognosis [8,9]. However, the transcriptional regulatory mechanisms of Twist1, especially its upstream regulatory networks, are not fully understood.

Recent studies have highlighted the important roles of RNA-binding proteins (RBPs) in tumor development and progression [10,11]. RBPs regulate gene expression with precision across various levels, including mRNA stability, splicing, localization, and translation. They are integral to processes such as tumor cell proliferation, apoptosis, metastasis, and drug resistance [12]. Traditional concepts indicate that RBPs primarily regulate gene expression at the post-transcriptional level. However, emerging evidence shows that many RBPs also have DNA-binding capabilities and can directly engage in transcriptional regulatory processes, acting as crucial links between transcriptional and post-transcriptional regulation [13,14].

The far upstream element binding protein (FUBP) family, as a single-strand DNA/RBP family, comprises three members: FUBP1, FUBP2, and FUBP3, which regulate gene transcription through recognition of purine-rich Far Upstream Element sequences (FUSE) [15,16]. Members of the FUBP family were first identified for their role in regulating c-myc proto-oncogene expression; however, later research has demonstrated that their regulatory networks are significantly more intricate than previously thought [17,18]. The oncogenic role of FUBP1 in various tumors has been extensively validated, whereas functional studies of FUBP2 and FUBP3 have lagged, especially those about the mechanistic roles of these proteins in tumor metastasis processes [19–21]. FUBP3, also known as FBP3, is a relatively understudied member of the FUBP family [22]. The FUBP3 protein comprises four K homology domains, can bind single-strand DNA and RNA and is primarily localized in the cell nucleus [22,23]. Bioinformatics analysis indicates abnormal FUBP3 expression in multiple tumor types, suggesting its potentially essential role in tumor progression [23–25]. The roles and molecular mechanisms of FUBP3 in tumor biology are not yet comprehensively investigated, in contrast to those of FUBP1, and the role of FUBP3 in the regulation of EMT-related gene expression and its specific functions in tumor metastasis processes remain unclear. This research gap limits our understanding of the complete roles of the FUBP family in tumor development and progression.

Signal transducer and activator of transcription 3 (STAT3) is a key component of the Janus kinase (JAK)–STAT signaling pathway, playing an important role in tumor cell proliferation, angiogenesis, and metastasis [26,27]. The persistent activation of STAT3 is an important characteristic of various malignant tumors [28,29]. Gene transcriptional regulation depends on the formation of transcriptional complexes formed by various regulatory molecules, including transcription factors, co-activators, and RBPs [30]. RBPs can serve as "scaffold" proteins, facilitating the recruitment of additional transcriptional regulatory factors and establishing intricate regulatory networks [31–33]. The mechanism of multiprotein complex formation is crucial in the regulation of genes associated with tumor metastasis. Bioinformatics analysis revealed that FUBP3 is highly expressed in lung cancer tissues and correlates with poor patient prognosis. Further analysis suggests that FUBP3 is involved in the regulation of genes associated with EMT. FUBP3 and STAT3 demonstrate a correlation in expression within tumor samples, indicating a possible functional relationship between them.

We hypothesized that FUBP3 facilitate lung cancer EMT and metastasis by recruiting STAT3 to form transcriptional complexes, thereby activating the transcription of Twist1. This study aims to elucidate the mechanistic role of FUBP3 in lung cancer metastasis, focusing on its interaction with STAT3 and the regulation of Twist1 expression. We validated the effects of FUBP3 on EMT and metastasis in lung cancer through *in vitro* and *in vivo* functional experiments. The interactions between FUBP3 and STAT3 and their role in the transcriptional regulation of Twist1 were explored using molecular biology techniques. Additionally, the therapeutic potential of targeting this regulatory axis was evaluated.

2. Methods

2.1 Bioinformatics and Database Analysis

Transcriptomic sequencing data for non-small cell lung cancer (NSCLC) were downloaded from The Cancer Genome Atlas (TCGA) database, including tumor tissue samples and paired normal tissue samples from lung adenocarcinoma (LUAD), and lung squamous cell carcinoma. Differential expression analysis was performed using R language (Version 4.2.0, R Core Team, R Foundation for Statistical Computing, Vienna, Austria) and the DESeq2 package (Version 1.36.0, Bioconductor, Fred Hutchinson Cancer Research Center, Seattle, WA, USA) to assess FUBP3 expression levels in tumor and normal tissues. Clinical follow-up data from patients with NSCLC in the TCGA cohort indicated that patients were divided into high- and low-expression groups according to the median FUBP3 expression level. Survival curves were plotted using the Kaplan–Meier method, and overall survival (OS) differences among groups were assessed using the Log-rank test. Functional enrichment analysis using Gene Ontology (GO) and pathway enrichment analysis via the Kyoto Encyclopedia of Genes and Genomes (KEGG) were performed using the Gene Denovo website (https://www.genedenovo.com/). A protein–protein interaction network for FUBP3 was established using the GeneMANIA protein interaction database (https://genemania.org/), and network visualization was performed using Cytoscape software (Version 3.8.2, The Cytoscape Consortium, University of California San Diego, San Diego, CA, USA). Immune score, stromal score, and tumor purity was calculated for each tumor sample with the ESTIMATE algorithm, and the relationship between FUBP3 expression and the tumor microenvironment was analyzed. The relative abundance of immune cell subsets was inferred using the CIBERSORT deconvolution al-

gorithm, and the effects of FUBP3 expression on tumor immune infiltration patterns were explored.

2.2 Clinical Sample Collection and Immunohistochemistry

Tissue specimens were collected from 30 patients with NSCLC who underwent surgical resection in the Department of Thoracic Surgery at our hospital between January 2025 and August 2025. This cohort included 30 cases of LUAD, which had paired adjacent normal tissues. Inclusion criteria: (1) pathologically confirmed primary NSCLC; (2) absence of preoperative chemotherapy, radiotherapy, or targeted therapy; (3) availability of complete clinicopathological data. Exclusion criteria: (1) concurrent malignancies; (2) severe cardiopulmonary insufficiency; (3) immunodeficiency diseases. All cases were diagnosed by qualified pathologists in accordance with the WHO classification criteria. This study received approval from the Hospital Ethics Committee of Liaocheng People's Hospital (approval number: 2025256), and all participants provided informed consent. Tissue specimens were promptly fixed in 4% paraformaldehyde (P1110, Beijing Solarbio Science & Technology Co., Ltd., Beijing, China) for 24 hours, subjected to gradient ethanol dehydration, paraffin embedded, and cut into create 4 µm-thick serial sections. The sections underwent deparaffinization in xylene (10023418, Sinopharm Chemical Reagent Co., Ltd., Shanghai, China), rehydration through a gradient of ethanol, and antigen retrieval by microwave heating in EDTA buffer (pH 8.0, ZLI-9069, Beijing Zhongshan Golden Bridge Biotechnology Co., Ltd., Beijing, China) for 15 minutes. The sections were washed with PBS (SH30256.01, HyClone Laboratories Inc., Logan, UT, USA) and treated with 3% H_2O_2 (H1009, Beijing Solarbio Science & Technology Co., Ltd., Beijing, China) for 10 minutes to block endogenous peroxidase activity. After blocking with 5% bovine serum albumin (SW3015, Beijing Solarbio Science & Technology Co., Ltd., Beijing, China) at room temperature for 1 hour, the sections were incubated overnight at 4 °C with the FUBP3 primary antibody (1:200, ab181111, Abcam plc, Cambridge, UK), washed with PBS, and incubated with horseradish peroxidase–conjugated goat anti-rabbit secondary antibody (1:500, PV-6001, Beijing Zhongshan Golden Bridge Biotechnology Co., Ltd., Beijing, China) at room temperature for 30 minutes. Color development was performed using a DAB chromogen kit (ZLI-9018, Beijing Zhongshan Golden Bridge Biotechnology Co., Ltd., Beijing, China), and the nuclei were counterstained with hematoxylin (G1140, Beijing Solarbio Science & Technology Co., Ltd., Beijing, China). The sections were dehydrated through with a gradient of ethanol, cleared in xylene, and subsequently mounted with neutral resin (G8590, Beijing Solarbio Science & Technology Co., Ltd., Beijing, China). Images were obtained using a Leica DM4000B microscope (Leica Microsystems GmbH, Wetzlar, Germany) and assessed independently by two pathologists employing a double-blind approach. Immunohistochemical staining was evaluated using a semiquantitative scoring system. The final score was determined by assessing staining intensity (0–3 points) and the percentage of positive cells (0–4 points), and a score of $\geq$4 points indicated positive expression.

2.3 Quantitative Real-Time Polymerase Chain Reaction

A549 and H460 cells were underwent various treatments were collected, and total RNA was extracted utilizing TRIzol reagent (15596018, Invitrogen, Thermo Fisher Scientific Inc., Waltham, MA, USA). The concentration and purity of RNA were assessed using a NanoDrop 2000 UV–Vis spectrophotometer (Thermo Fisher Scientific Inc., Waltham, MA, USA). Only samples exhibiting A260/A280 ratios within the range of 1.8–2.0 and A260/A230 ratios exceeding 2.0 were used for subsequent experiments. One microgram of total RNA was reverse-transcribed to synthesize cDNA using a PrimeScript RT reagent kit (RR047A, TaKaRa Bio Inc., Kusatsu, Shiga, Japan). The reaction conditions included incubation at 37 °C for 15 minutes, 85 °C incubation for five seconds, and subsequent storage at 4 °C. cDNA was used as a template for amplification, which was performed using a SYBR Premix Ex Taq kit (RR420A, TaKaRa Bio Inc., Kusatsu, Shiga, Japan) on an ABI 7500 real-time fluorescence quantitative PCR system. The PCR reaction system comprised a total volume of 20 µL, which included 10 µL of SYBR Premix Ex Taq, 0.4 µL of forward primer, 0.4 µL of reverse primer, 2 µL of cDNA template, and 7.2 µL of ddH_2O. The amplification program included an initial denaturation step at 95 °C for five minutes and 40 cycles of amplification comprising denaturation at 95 °C for 30 seconds, annealing at 60 °C for 30 seconds, and extension at 72 °C for 30 seconds. Then, product specificity was confirmed through melting curve analysis. Table 1 presents the primer sequences utilized in this study. The relative expression of target genes was calculated using the $2^{-\Delta\Delta Ct}$ method, and Glyceraldehyde-3-phosphate dehydrogenase (GAPDH) was used as the internal reference gene. Each sample was analyzed in triplicate.

2.4 Western Blot Analysis

Cells exposed to different treatments were collected, washed with PBS, and lysed using prechilled RIPA lysis buffer (R0020, Beijing Solarbio Science & Technology Co., Ltd., Beijing, China). The samples were then incubated on ice for 30 minutes with intermittent vortexing. Supernatants were collected following centrifugation at 12,000 rpm for 15 minutes at 4 °C. Protein concentrations were determined using the BCA protein assay kit (PC0020, Beijing Solarbio Science & Technology Co., Ltd., Beijing, China). Protein samples were combined with 5×SDS-PAGE loading buffer (P1015, Beijing Solarbio Science & Technology Co., Ltd., Beijing, China) and denatured by boiling at 100 °C for 5 minutes. Equal quantities of protein sam-

Table 1. Primer sequences used in this study.

Gene	Forward Primer (5′–3′)	Reverse Primer (5′–3′)
GAPDH	GGAGCGAGATCCCTCCAAAAT	GGCTGTTGTCATACTTCTCATGG
STAT3	CAGCAGCTTGACACACGGTA	AAACACCAAAGTGGCATGTGA
Twist1	GGAGTCCGCAGTCTTACGAG	TCTGGAGGACCTGGTAGAGG
FUBP3	GCAAGGTCATCCATGACAACTC	CTCCTTCTGCATCCTGTCAAAC

GAPDH, Glyceraldehyde-3-phosphate dehydrogenase; *STAT3*, Signal transducer and activator of transcription 3; *Twist1*, Twist family BHLH transcription factor 1; *FUBP3*, Far upstream element binding protein 3.

ples (30 µg) were resolved by SDS-PAGE employing a 10% polyacrylamide separating gel. After electrophoresis, proteins were transferred to PVDF membranes (IPVH00010, Millipore Corporation, Burlington, MA, USA) using the wet transfer method at a constant voltage of 100 V for a duration of 90 minutes. Membranes were incubated with 5% nonfat milk powder (A8120, Beijing Solarbio Science & Technology Co., Ltd., Beijing, China) at room temperature for 1 hour, followed by three washes with TBST buffer (T8220, Beijing Solarbio Science & Technology Co., Ltd., Beijing, China) for 10 minutes each. Membranes were incubated overnight at 4 °C with primary antibodies, including FUBP3 (1:1000, ab181111, Abcam plc, Cambridge, UK), STAT3 (1:1000, #9139, Cell Signaling Technology Inc., Danvers, MA, USA), E-cadherin (1:1000, #3195, Cell Signaling Technology Inc., Danvers, MA, USA), vimentin (1:1000, ab92547, Abcam plc, Cambridge, UK), and GAPDH (1:2000, ab181602, Abcam plc, Cambridge, UK). After TBST washing, the membranes were incubated with the appropriate horseradish peroxidase-conjugated secondary antibodies (horseradish peroxidase-conjugated goat anti-rabbit IgG (1:10,000, ZB-2301, Beijing Zhongshan Golden Bridge Biotechnology Co., Ltd., Beijing, China); horseradish peroxidase-conjugated goat anti-mouse IgG (1:10,000, ZB-2305, Beijing Zhongshan Golden Bridge Biotechnology Co., Ltd., Beijing, China) at room temperature for 2 hours. The membranes were washed again with TBST and then developed using enhanced chemiluminescence kit (PE0010, Beijing Solarbio Science & Technology Co., Ltd., Beijing, China). Images were captured using a ChemiDoc XRS+ imaging system (Bio-Rad Laboratories Inc., Hercules, CA, USA). Protein band gray values were analyzed with ImageJ software (Version 1.53e, National Institutes of Health, Bethesda, MD, USA) and normalized to GAPDH as the internal reference protein, and results were presented as the ratio of target protein to the gray values of internal reference protein.

2.5 Co-Immunoprecipitation (Co-IP)

A549 cells were harvested 48 hours after transfection through centrifugation at 800 rpm for 3 minutes at 4 °C. The supernatant was removed, and the cells were washed twice with prechilled PBS. PBS was completely removed, and the cell pellets were preserved. Cells were resuspended in prechilled immunoprecipitation lysis buffer (R0020, Beijing Solarbio Science & Technology Co., Ltd., Beijing, China) and homogenized 30–50 times with a glass homogenizer. The samples were centrifuged at 12,000 rpm for 5 minutes, and supernatants were collected as cell lysates. Protein concentrations were determined using a BCA protein assay kit (Beijing Solarbio, PC0020), and 500 µg of total protein was used for each reaction. Cell lysates were separated into forward and reverse co-immunoprecipitation groups. Each group received 1 µg of FUBP3 antibody (Abcam, ab181111), STAT3 antibody (Cell Signaling Technology, #9139), or a negative control IgG antibody (#2729, Cell Signaling Technology Inc., Danvers, MA, USA) overnight and incubated overnight with gentle rocking at 4 °C. This setup included three conditions: (1) Input (whole cell lysate), (2) IgG negative control (beads plus nonspecific antibody), and (3) Experimental Groups (with Anti-FUBP3 or Anti-STAT3 antibodies). Buffer-pretreated protein A/G magnetic beads (10 µL, SE101, Beijing Solarbio Science & Technology Co., Ltd., Beijing, China) or agarose beads (10 µL, sc-2003, Santa Cruz Biotechnology Inc., Dallas, TX, USA) were subsequently added, and the samples were incubated with gentle rocking at 4 °C for 2–4 hours. Following immunoprecipitation, samples underwent centrifugation at 12,000 rpm for 30 seconds at 4 °C to pellet the beads. The supernatant was aspirated, and the beads were washed three or four times with 1 mL of lysis buffer, centrifuging at 1000 rpm for 1 minute at 4 °C each time. Subsequently, 15–20 µL of 1 $\times$ SDS loading buffer (Beijing Solarbio, P1015) was added, and the samples were subjected to boiling at 100 °C for 5 minutes to elute the bound protein complexes. The samples were eluted and separated using 10% SDS-PAGE and characterized through immunoblot analysis in accordance with standard Western blot procedures.

2.6 Immunofluorescence Staining

After cell digestion, cells were placed onto sterile coverslips that had been prepositioned in 48-well plates at a density of 5 $\times$ 10^4 cells per well. Following overnight cell attachment, corresponding treatments were administered. The cells underwent three washes with prechilled PBS and then fixed using 4% paraformaldehyde (Beijing Solarbio, P1110) at room temperature for 20 minutes, washed with

PBS, and permeabilized with 0.1% Triton X-100 (T8200, Beijing Solarbio Science & Technology Co., Ltd., Beijing, China) at room temperature for 10 minutes. The cells were then incubated with a 5% goat serum blocking solution (SL038, Beijing Solarbio Science & Technology Co., Ltd., Beijing, China) at room temperature for 1 hour to prevent nonspecific binding. After the removal of the blocking solution, primary antibodies were introduced, including FUBP3 (Abcam, ab181111, 1:200 dilution), STAT3 (Cell Signaling Technology, #9139, 1:200 dilution), Twist1 (1:200, ab323385, Abcam plc, Cambridge, UK), E-cadherin (Cell Signaling Technology, #3195, 1:300 dilution), and vimentin (Abcam, ab92547, 1:200 dilution). Incubation was performed overnight at 4 °C in a humidified chamber. After three washes with PBS, either the Alexa Fluor-488-conjugated goat anti-rabbit IgG secondary antibody (Abcam, ab150077, 1:1000 dilution) or Alexa Fluor-594-conjugated goat anti-mouse IgG secondary antibody (1:1000, ab150116, Abcam plc, Cambridge, UK) was applied. Incubation occurred at room temperature in the dark for 2 hours. Nuclei were counterstained with 4′,6-diamidino-2-phenylindole (DAPI, 1:1000, C0065, Beijing Solarbio Science & Technology Co., Ltd., Beijing, China) at room temperature in the dark for 5 minutes. Coverslips were subsequently mounted using an anti-fade mounting medium (S2100, Beijing Solarbio Science & Technology Co., Ltd., Beijing, China), and images were observed and captured with a fluorescence microscope (Olympus IX73, Olympus Corporation, Tokyo, Japan).

2.7 Cell Culture and Lentiviral Transduction

A549 and H460 human NSCLC cell lines were acquired from the Cell Bank of the Chinese Academy of Sciences and subsequently seeded in culture dishes. All cell lines were validated by STR profiling and were confirmed to be negative for mycoplasma contamination. Cells were cultured in RPMI-1640 complete medium (SH30809.01, HyClone Laboratories Inc., Logan, UT, USA) supplemented with 10% fetal bovine serum (10099-141, Gibco, Thermo Fisher Scientific Inc., Waltham, MA, USA), 100 U/mL penicillin, and 100 µg/mL streptomycin (SV30010, HyClone Laboratories Inc., Logan, UT, USA). They were maintained in a sterile incubator (Thermo Fisher Scientific Inc., Waltham, MA, USA) at 37 °C with 5% CO_2 until they reached the logarithmic growth phase. Upon reaching a cell density of approximately 80%, the culture medium was aspirated, and the cells were washed twice with sterile PBS (Hyclone, SH30256.01). One milliliter of trypsin–EDTA digestion solution (25200-072, Gibco, Thermo Fisher Scientific Inc., Waltham, MA, USA) was applied to digest cells for 2–3 minutes until the cells rounded and detached. Digestion was halted by the addition of 2 mL complete medium. Cells were gently pipetted to create a cell suspension, which was then transferred to a 15 mL centrifuge tube and centrifuged at 1000 rpm for 5 minutes. After the removal of the supernatant, cells were resuspended in 2 mL of complete medium and passaged at a 1:3 ratio into new culture dishes. Six milliliters of complete medium were added to each dish, mixed thoroughly, and subsequently returned to the incubator for ongoing culture.

The construction and infection of the FUBP3 shRNA lentiviral vector were conducted in accordance with the specified instructions. The control sequence was a scrambled nonspecific sequence, which was cloned into the pLKO.1 lentiviral vector (#8453, Addgene Inc., Watertown, MA, USA). The vector plasmid was co-transfected with the packaging plasmid psPAX2 (#12260, Addgene Inc., Watertown, MA, USA) and the envelope plasmid pMD2.G (#12259, Addgene Inc., Watertown, MA, USA) in a ratio of 4:3:1 into 293T cells with Lipofectamine 3000 reagent (L3000015, Invitrogen, Thermo Fisher Scientific Inc., Waltham, MA, USA) for transfection. The supernatant containing the virus was collected 48 hours after transfection, filtered using a 0.45 µm membrane, and subsequently stored at –80 °C for future applications. A549, H1299, and H460 cells were cultured in six-well plates and subsequently infected with lentivirus upon achieving a cell density of 50%–60%. Cells were categorized into the NC group (negative control group, infected with scrambled shRNA lentivirus) and the FUBP3-shRNA group (infected with FUBP3 shRNA lentivirus), utilizing a multiplicity of infection of 10. Fresh medium was replaced 24 hours after infection, and following an additional 48 hours of culture, puromycin (2 µg/mL, P8230, Beijing Solarbio Science & Technology Co., Ltd., Beijing, China) was introduced for the selection of positive clones. Selection persisted for one to two weeks until stable transfected cell lines were established, and the efficiency of FUBP3 knockdown was confirmed via Western blot analysis. The complete human FUBP3 cDNA was inserted into the pcDNA3.1(+) vector (Invitrogen, Thermo Fisher Scientific Inc., Waltham, MA, USA). Four synonymous nucleotide substitutions were introduced into the shRNA recognition sequence through site-directed mutagenesis to render the construct resistant to shRNA targeting, preserving the original amino acid coding while inhibiting shRNA binding. Cells with FUBP3 knockdown (A549-shFUBP3 and H460-shFUBP3) were transfected with either the shRNA-resistant FUBP3 plasmid or an empty vector control using Lipofectamine 3000 (Invitrogen). This procedure was followed by G418 selection at a concentration of 800 µg/mL for 3 weeks. The successful restoration of FUBP3 expression was confirmed by Western blot analysis. The full-length human Twist1 cDNA was cloned into the pcDNA3.1(+) vector and transfected into A549 and H460 cells utilizing Lipofectamine 3000 (Invitrogen). Stable cell lines were selected using G418 (800 µg/mL), which was administered 3 weeks prior. Twist1 shRNA lentiviral constructs were developed utilizing the pLKO.1 backbone (Addgene, #8453). Lentivirus was generated through the co-transfection of 293T cells with a

shRNA plasmid, psPAX2 packaging plasmid, and pMD2.G envelope plasmid in a 4:3:1 ratio. Target cells were infected with the viral supernatant and were subsequently selected using puromycin (2 µg/mL), which was administered for 2 weeks. Knockdown efficiency was confirmed using quantitative real-time polymerase chain reaction. Scrambled shRNA served as the negative control.

2.8 Sphere Formation Assay

Forty-eight hours after lentiviral transduction, A549 and H460 cells were digested into single-cell suspensions and seeded at a density of 1000 cells per well in ultralow attachment six-well plates (3471, Corning Inc., Corning, NY, USA). Cells were cultured in a serum-free sphere culture medium composed of DMEM/F12 (SH30023.01, HyClone Laboratories Inc., Logan, UT, USA). Cultures were incubated at 37 °C with 5% CO_2 for 10–14 days, and half of the medium was replaced every 3 days. Following the completion of culture, the cytoskeleton was stained with phalloidin–FITC (1:200, P5282, Sigma-Aldrich LLC, St. Louis, MO, USA) for 30 minutes and washed with PBS, and the nuclei were stained with DAPI (1:1000, C0065, Beijing Solarbio Science & Technology Co., Ltd., Beijing, China) for 5 minutes. Images were observed and captured under a laser confocal microscope (Leica TCS SP8, Leica Microsystems GmbH, Wetzlar, Germany).

2.9 Transwell Assay

Serum-free RPMI-1640 medium was introduced into the upper chamber of Transwell inserts for cell migration assays. Co-cultured A549 cells were suspended in a serum-free medium at a concentration of 5×10^6 cells/mL and subsequently seeded into the upper chamber at 200 µL per well. Meanwhile, 500 µL of complete medium added to the lower chamber. Cells were incubated at 37 °C for 24 hours. Following three washes with PBS, cells were fixed using 4% paraformaldehyde for 10 minutes, subsequently washed three additional times with PBS, and then stained with 0.1% crystal violet for 15 minutes. After washing and air-drying, the cells were examined microscopically. Three distinct fields of view were randomly selected for photography and cell counting, and the average was calculated. The number of migrated cells in each group was documented and subjected to statistical analysis. In cell invasion assays, 100 µL of Matrigel was initially added to the upper chamber of Transwell inserts and incubated at 37 °C for 30 minutes. The subsequent steps were identical to those employed in cell migration assays.

2.10 EdU Cell Proliferation Assay

After cell treatment, 100 µL of EdU medium (50 µmol/L) was added to each well and incubated for 2 hours. Cells underwent three washes with phosphate buffer, fixed in 4% paraformaldehyde at room temperature for 30 minutes, and treated with 0.5% Triton X-100 for 10 minutes. After washing with phosphate buffer, Apollo staining solution was introduced and incubated with agitation at room temperature in the dark for 30 minutes. Nuclei were stained using a DAPI solution (5 µg/mL). Immediately after staining, the cells were observed under a microscope, and five random fields of view selected for counting. The EdU-positive cell rate for each group was determined using ImageJ software (Version 1.8, National Institutes of Health, Bethesda, MD, USA). The rate of EdU-positive cells was calculated as follows: (number of EdU-positive cells/total number of cells) × 100%.

2.11 TUNEL Apoptosis Assay

Following the transfection treatment of each cell group, cells were fixed using 4% paraformaldehyde fixative (Beijing Solarbio, P1110) at room temperature for a duration of 30 minutes. After PBS washing, a permeabilization solution (0.1% Triton X-100, Beijing Solarbio, T8200) was introduced to resuspend the cells and incubated at room temperature for 5 minutes. The samples were then washed with PBS three times, and 50 µL of the TUNEL reaction mixture was added to each sample. The mixture was supplied by the TUNEL assay kit (Roche, 11684795910) and included TdT enzyme and fluorescently labeled dUTP. After incubation at 37 °C in the dark for 60 minutes, the cells were washed three times with PBS. Coverslips were mounted with antifade mounting medium (Beijing Solarbio, S2100) and examined with a fluorescence microscope (Olympus IX73). TUNEL-positive cells exhibited red fluorescence (excitation wavelength 550 nm, emission wavelength 570 nm), while DAPI-stained nuclei displayed blue fluorescence. The rate of TUNEL-positive expression was determined by the formula (number of TUNEL-positive cells/total number of DAPI-positive cells × 100%).

2.12 Cytoskeletal Staining

A549 and H460 cells were cultured in 24-well plates containing prepositioned sterile coverslips and subsequently stained upon reaching 70% confluence. Cells were fixed using 4% paraformaldehyde (Beijing Solarbio, P1110) at room temperature for 30 minutes, permeabilized with 0.1% Triton X-100 (Beijing Solarbio, T8200) for 30 minutes, and subsequently blocked with 5% BSA (A8010, Beijing Solarbio Science & Technology Co., Ltd., Beijing, China) at room temperature for 1 hour to minimize non-specific binding. Following the removal of the blocking solution, phalloidin–FITC (Sigma-Aldrich, P5282) was applied at a dilution of 1:1000 in 1% BSA–PBS and incubated overnight at 4 °C in the dark within a humidified chamber. Nuclei were stained using a DAPI staining solution (Beijing Solarbio, C0065, 1:1000) at room temperature in the dark for a duration of 10 minutes. Coverslips were mounted using anti-fade mounting medium (Beijing Solarbio, S2100) and examined with a laser confocal microscope (Leica TCS SP8). The excitation wavelength for FITC was 488 nm,

indicating green fluorescence associated with F-actin, and DAPI was excited at 358 nm, revealing blue fluorescence corresponding to nuclei.

2.13 Scanning Electron Microscopy (SEM)

Sterile coverslips were initially positioned in culture flasks, followed by the seeding and culturing of cells until monolayer confluence was achieved, at which point the coverslips were removed. Cells were fixed with 2.5% glutaraldehyde (Beijing Solarbio, G1102) at 4 °C for 2 hours, followed by secondary fixation with 1% osmium tetroxide (Sigma-Aldrich, 75632) at room temperature for 1 hour. Cells underwent sequential dehydration in 30%, 50%, 70%, 80%, 90%, 95%, and 100% ethanol for 15 minutes at each concentration, and 100% ethanol dehydration was performed twice. After dehydration, CO_2 critical point drying was conducted using the Leica EM CPD300, and subsequently, gold sputter coating was applied in a vacuum coating unit, achieving a thickness of approximately 10–15 nm. Samples were examined for cell surface morphology using a HITACHI S-570 scanning electron microscope, operating at an accelerating voltage of 15 kV and a working distance of 10–15 mm.

2.14 Nude Mouse Tail Vein Injection Metastasis Model

This research received approval from the Institutional Animal Care and Use Committee of Liaocheng People's Hospital (approval number: 2025257). Female BALB/c nude mice (SPF grade; 5–6 weeks old; 20–22 g body weight) were obtained from Beijing Vital River Laboratory Animal Technology Co., Ltd. (Laboratory Animal Production License No. SCXK(Jing)2016-0011). Nude mice were maintained in a specific pathogen-free barrier system at an environmental temperature of 25 $\pm$ 1 °C and relative humidity of 50%–70%. They were subjected to a 12-hour light/dark cycle, housed at a density of five mice per cage, and provided with ad libitum access to food and water. The acclimatization period was 1 week. The experiment comprised six mice per group. Mice underwent a 12-hour fasting period prior to the experiment. A549 cells that were transfected were resuspended in serum-free RPMI-1640 medium, with the cell concentration adjusted to 5 $\times$ 10^6 cells/mL. Nude mice were placed in a specialized restraint device, and the tail vein region was cleansed with 75% alcohol to facilitate blood vessel dilation. The needle was inserted at a 45° angle using a 1 mL sterile syringe. After entry into the tail vein, a 200 µL cell suspension (1 $\times$ 10^6 cells/mouse) was administered at a consistent rate. Following injection, mouse body weight, food intake, and overall condition were assessed weekly to identify symptoms including respiratory distress, decreased activity, and weight loss. Mice were anesthetized using pentobarbital sodium (Nembutal, 50 mg/kg body weight, intraperitoneal injection). The anesthetic solution was prepared by diluting pentobarbital sodium stock solution (50 mg/mL, Sigma-Aldrich, P3761) in sterile physiological saline to achieve the appropriate concentration based on individual mouse body weight. Six weeks after injection, mice were euthanized using CO_2 delivered at a flow rate of 1 L/min, with CO_2 concentration gradually increased from 30% to 100% over 2–3 minutes according to American Veterinary Medical Association (AVMA) guidelines. Bilateral lung tissues were excised, fixed in 10% neutral formalin, paraffin-embedded, and subjected to HE staining to assess the number, size, and distribution of pulmonary metastatic foci. Metastatic foci numbers were quantified using Image-Pro Plus software.

2.15 HE Staining of Pulmonary Metastatic Foci

Lung tissues were fixed in 10% neutral formalin for 24 hours, followed by routine dehydration and paraffin embedding to prepare 4 µm serial sections. The steps for HE staining were as follows: Sections were deparaffinized to water, stained with hematoxylin for 5 minutes, rinsed with tap water to eliminate excess dye, differentiated with 1% hydrochloric acid–alcohol solution for several seconds until nuclei became clear, blued with ammonia water for 10 seconds, and rinsed with running water for 10 minutes. After staining with 1% eosin for 3 minutes, the sections underwent sequential dehydration in 85%, 95%, and 100% ethanol for 2 minutes each, were cleared in xylene for two 5-minute intervals, and were subsequently mounted with neutral resin. The morphological characteristics of the pulmonary metastatic foci were examined using an optical microscope (Olympus BX53, Olympus Corporation, Tokyo, Japan), and metastatic foci were counted.

2.16 Proximity Ligation Assay (PLA)

The proximity ligation assay (PLA) was performed using the Duolink PLA Technology (Sigma-Aldrich, DUO92101) in accordance with the manufacturer's guidelines. A549 cells were plated on sterile coverslips in 48-well plates at a density of 5 $\times$ 10^4 cells per well and incubated overnight. Cells were fixed using 4% paraformaldehyde (Beijing Solarbio, P1110) for 20 minutes at room temperature, permeabilized with 0.1% Triton X-100 (Beijing Solarbio, T8200) for 10 minutes, and subsequently blocked with Duolink blocking solution for 1 hour at 37 °C. Primary antibodies FUBP3 (1:200, ab181111, Abcam plc, Cambridge, UK) and STAT3 (1:200, #9139, Cell Signaling Technology Inc., Danvers, MA, USA) were incubated overnight at 4 °C. Following PBS washing, cells were incubated with PLA PLUS and MINUS oligonucleotide-conjugated secondary antibodies for 1 hour at 37 °C. The ligation reaction was conducted for 30 minutes at 37 °C, subsequently followed by amplification for 100 minutes at the same temperature. Nuclei were counterstained using DAPI (Beijing Solarbio, C0065, diluted 1:1000). Fluorescence microscopy (Olympus IX73, Olympus Corporation, Tokyo, Japan) was employed to capture images, revealing

PLA signals (red fluorescent dots) that indicate protein–protein interactions within a 40 nm range.

2.17 Statistical Analysis

Experimental data were analyzed utilizing SPSS 26.0 (IBM Corporation, Armonk, NY, USA) and GraphPad Prism 10.0 (GraphPad Software LLC, Boston, MA, USA) statistical software. Results are presented as mean $\pm$ standard deviation ($\bar{x} \pm$ s) derived from a minimum of three independent biological replicates, unless otherwise indicated in the figure legends. The independent samples *t*-test facilitated comparisons between two groups, while one-way analysis of variance (ANOVA) was employed for comparisons among multiple groups. Tukey's post hoc test was utilized for pairwise comparisons between groups. p values less than 0.05 were considered statistically significant ($^{*}p < 0.05$, $^{**}p < 0.01$, $^{***}p < 0.001$).

3. Results

3.1 Elevated FUBP3 Expression Correlates With Poor Survival Outcomes in Lung Cancer Patients

To identify key regulators of lung cancer metastasis, we focused on FUBP3 through bioinformatics screening (Fig. 1A). Single-cell analysis revealed FUBP3 upregulation in mesenchymal-type lung cancer cells, suggesting its involvement in mesenchymal transformation (Fig. 1B). TCGA database analysis confirmed elevated FUBP3 transcription in lung cancer versus normal tissues ($p < 0.01$; Fig. 1C). Immunohistochemical analysis of 30 paired patient samples validated higher FUBP3 protein expression in tumor versus adjacent normal tissues (Fig. 1D,E). Further analysis showed that FUBP3 expression levels positively correlated with genomic heterogeneity in lung cancer, with tumor samples exhibiting high FUBP3 expression demonstrating higher genomic instability (Fig. 1F). Cancer stem cell correlation analysis indicated that FUBP3 expression is closely associated with stemness characteristics of lung cancer cells, with increased enrichment of stem cell markers in tumor samples with high FUBP3 expression (Fig. 1G). Clinicopathological analysis revealed important associations between FUBP3 expression and lung cancer invasive and metastatic capabilities. FUBP3 protein expression levels in M1 stage (distant metastasis) lung cancer patients were higher than those in M0 stage (no distant metastasis) patients ($p < 0.01$), indicating that FUBP3 expression is directly related to lung cancer metastatic capacity (Fig. 1H). Analysis across different T stages showed that FUBP3 expression exhibited an upward trend with increasing tumor T stage, confirming a positive correlation between FUBP3 expression and local tumor invasive capacity (Fig. 1I). Kaplan–Meier survival analysis demonstrated that FUBP3 expression levels are closely associated with lung cancer patient prognosis. Patients were grouped according to the median FUBP3 expression level, and results showed that patients with high FUBP3 expression had shorter overall survival than those with low expression (Fig. 1J). FUBP3 expression correlated with immune regulatory genes and immune checkpoint molecules while negatively correlating with immune activation molecules, suggesting association with an immunosuppressive microenvironment (**Supplementary Fig. 1A,B**). These findings establish FUBP3 as aberrantly expressed in lung cancer, closely associated with tumor invasion, metastasis, genomic instability, stemness, and poor prognosis, supporting its potential as a prognostic biomarker.

3.2 FUBP3 Drives Lung Cancer Progression by Promoting Metastasis

To investigate the functional role of FUBP3 in lung cancer cells, we first examined FUBP3 expression levels in different lung cancer cell lines. Western blot analysis showed that compared to human bronchial epithelial cells BEAS-2B, FUBP3 was universally highly expressed in lung cancer cell lines, with the highest expression in A549 cells (approximately 4-fold), followed by H460 cells (approximately 3-fold), and relatively lower expression in PC-9 cells (approximately 1.2-fold) (Fig. 2A). Based on these results, we selected FUBP3 high-expressing A549 and H460 cell lines for subsequent functional studies. To explore the functional role of FUBP3 in lung cancer progression, we constructed stable FUBP3 knockdown A549 and H460 cell lines and established rescue cell lines to verify phenotype specificity. Western blot analysis confirmed transfection efficiency, with FUBP3 protein levels in the sh-FUBP3 group decreased compared to the control group, while FUBP3 expression was effectively restored in the shRNA-rescue group (Fig. 2B). Clonogenic sphere formation assays demonstrated that FUBP3 knockdown suppressed the proliferative potential and sphere-forming capacity of A549 and H460 cells. Compared to the control group, the sh-FUBP3 group formed significantly fewer clonogenic spheres with reduced sphere volume, while cell sphere-forming capacity was partially restored after rescuing FUBP3 expression (Fig. 2C). These results indicate that FUBP3 plays an important role in maintaining lung cancer cell proliferative capacity and stem cell-like characteristics. To evaluate the effect of FUBP3 on lung cancer cell metastatic capacity, we performed Transwell migration and invasion assays. Migration assay results showed that FUBP3 knockdown inhibited the migration capacity of A549 and H460 cells, with fewer cells migrating through the Transwell membrane compared to the control group, while cell migration capacity was significantly restored after rescuing FUBP3 expression (Fig. 2D). Similarly, invasion assays demonstrated that FUBP3 knockdown weakened lung cancer cells' invasive capacity to penetrate Matrigel, with invasive cell numbers reduced by approximately 70–80% compared to the control group, and rescue experiments confirmed the FUBP3-dependence of this phenotype (Fig. 2E). To further elucidate the effects of FUBP3

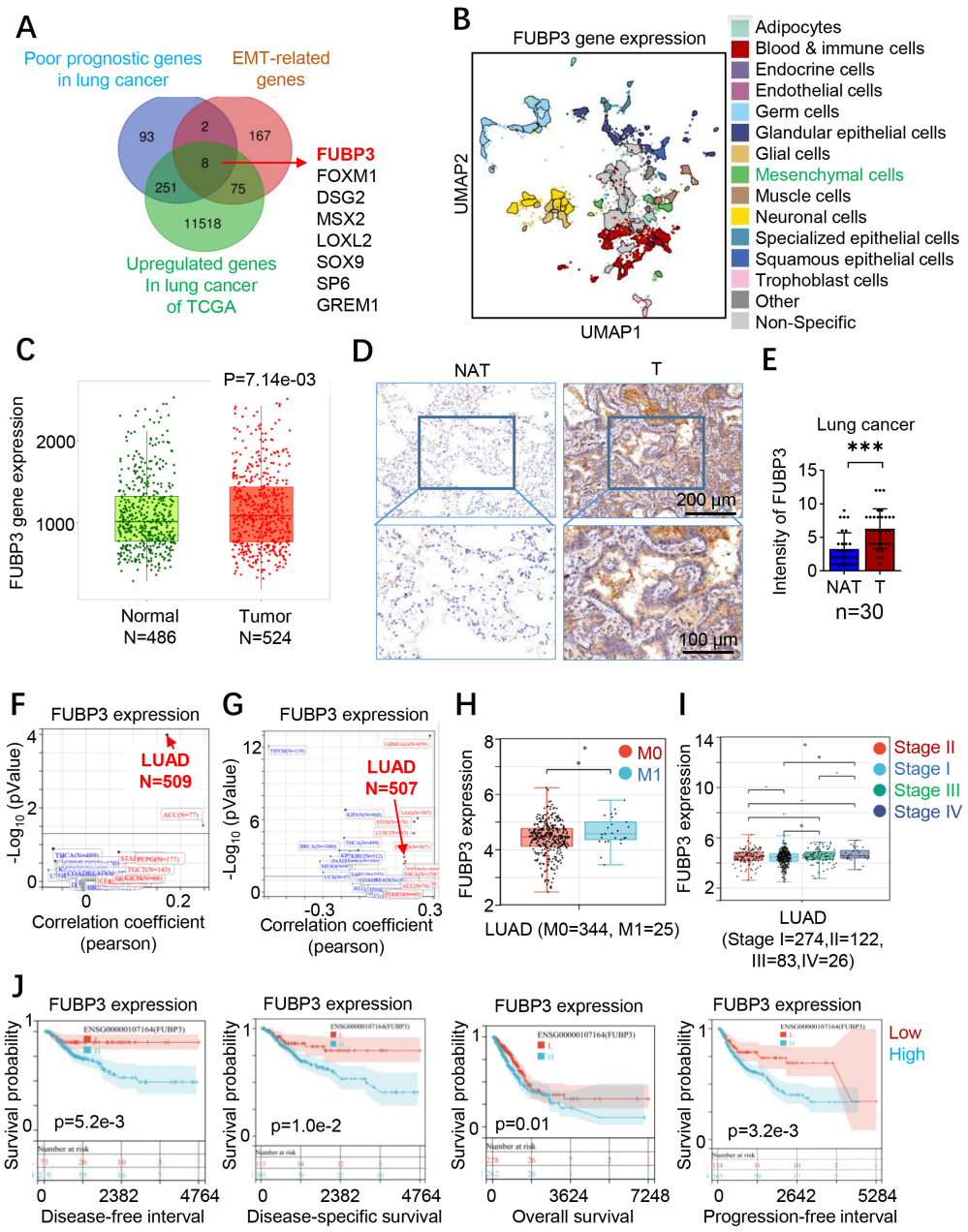

Fig. 1. Elevated FUBP3 expression correlates with poor survival outcomes in lung cancer patients. (A) Venn diagram showing the bioinformatics screening strategy for identifying poor prognostic genes and EMT-related genes in lung cancer, with FUBP3 among the overlapping candidates. (B) UMAP plot from single-cell RNA sequencing analysis demonstrating FUBP3 upregulation in mesenchymal cell populations within lung cancer tissues ($p = 7.14 \times 10^{-3}$). (C) TCGA database analysis showing significantly elevated FUBP3 expression in lung cancer tissues (N = 524) compared to normal tissues (N = 486). (D,E) Representative immunohistochemical staining images (D) and quantitative analysis. Scale bar: 100 μm and Scale bar: 200 μm. (E) of FUBP3 expression in paired lung cancer and normal adjacent tissues (NAT) (n = 30 per group). (F) Correlation heatmap showing positive associations between FUBP3 expression and genomic heterogeneity markers in LUAD patients (N = 509). (G) Correlation analysis demonstrating positive correlation between FUBP3 expression and cancer stem cell markers in LUAD patients (N = 507). (H) Box plot comparing FUBP3 expression levels between M0 (N = 344) and M1 (N = 25) stage LUAD patients. (I) FUBP3 expression levels across different T stages in LUAD patients (Stage I = 274, II = 122, III = 83, IV = 26). (J) Kaplan–Meier survival curves showing associations between FUBP3 expression and disease-free interval ($p = 5.2 \times 10^{-3}$), disease-specific survival ($p = 1.0 \times 10^{-2}$), overall survival ($p = 0.01$), and progression-free interval ($p = 3.2 \times 10^{-3}$). Data are presented as mean ± SD. *$p < 0.05$, ***$p < 0.001$. "+" indicates the presence of a treatment, while "–" indicates the absence of a treatment.

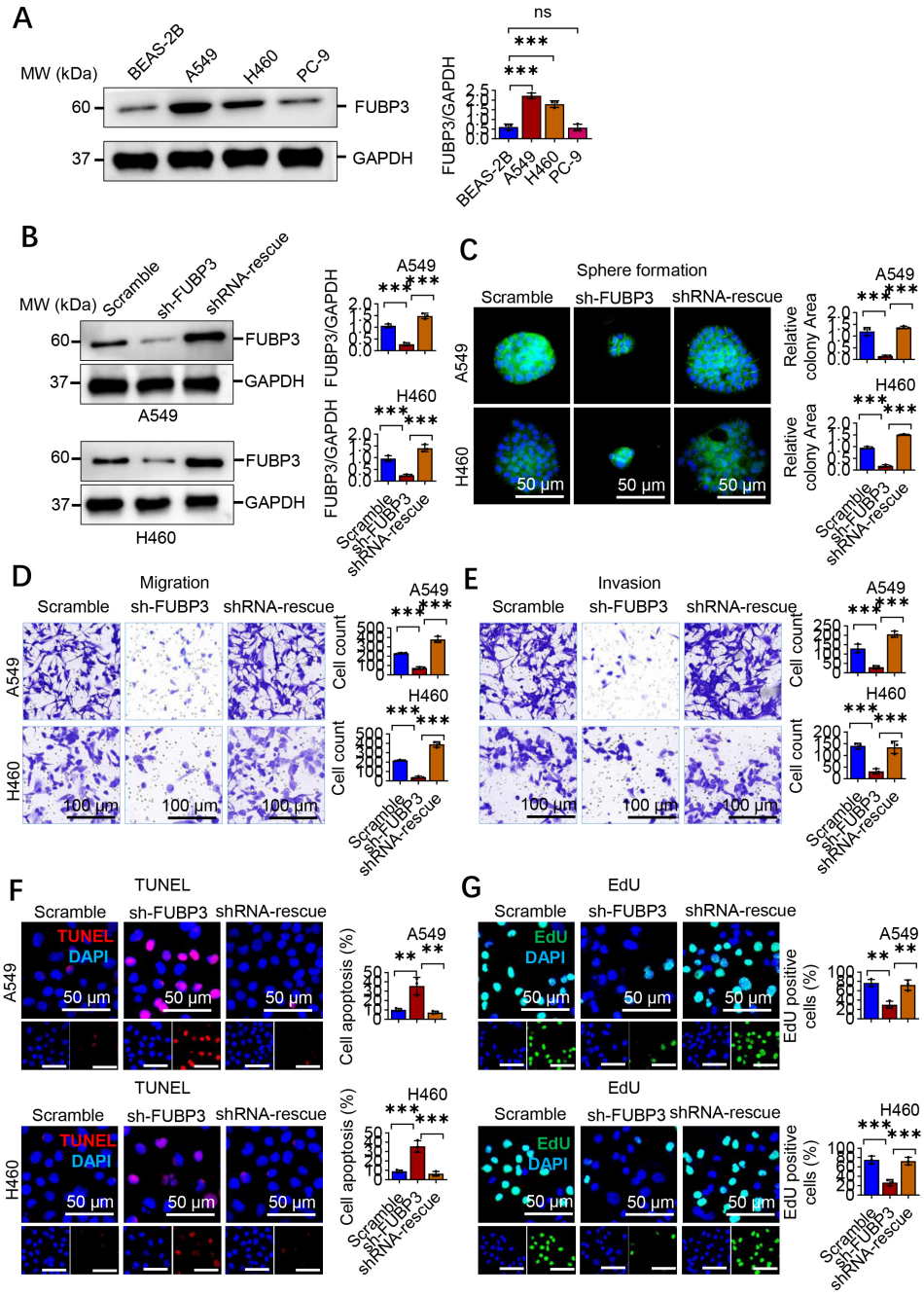

Fig. 2. FUBP3 drives lung cancer progression by promoting metastatic potential. (A) Western blot analysis of FUBP3 protein levels in lung cancer cell lines (A549, H1299, H460) compared to normal lung epithelial cells (BEAS-2B). GAPDH served as loading control. (B) Western blot confirmation of FUBP3 knockdown and rescue efficiency in A549 and H460 cell lines. (C) Sphere formation assay evaluating self-renewal capacity in A549 and H460 cells following FUBP3 manipulation. Scale bar: 50 μm. (D) Transwell migration assay assessing migratory capacity of FUBP3-modified A549 and H460 cells. Scale bar: 100 μm. (E) Transwell invasion assay evaluating invasive potential of A549 and H460 cells with FUBP3 knockdown and rescue. Scale bar: 100 μm. (F) TUNEL staining analysis of apoptotic cell death in FUBP3-modified A549 and H460 cells. TUNEL-positive cells (red), nuclei (blue, DAPI). Scale bar: 50 μm. (G) EdU incorporation assay measuring cell proliferation in A549 and H460 cells following FUBP3 manipulation. EdU-positive cells (green), nuclei (blue, DAPI). Scale bar: 50 μm. Data are presented as mean ± SD from three independent biological replicates (n = 3). Statistical comparisons were performed using one-way ANOVA followed by Tukey's post hoc test. ns, not significant, $^{**}p < 0.01$, $^{***}p < 0.001$.

knockdown on cellular biological behaviors, we examined cell apoptosis and proliferation status. TUNEL staining results showed that FUBP3 knockdown induced lung cancer cell apoptosis, with the proportion of TUNEL-positive cells increased approximately 3-fold compared to the control group, while cell apoptosis levels were significantly reduced after rescuing FUBP3 expression (Fig. 2F). These results indicate that FUBP3 possesses anti-apoptotic functions and contributes to lung cancer cell survival. EdU proliferation assays further confirmed FUBP3's regulatory role in cell proliferation. Results showed that FUBP3 knockdown inhibited DNA synthesis capacity in A549 and H460 cells, with the proportion of EdU-positive cells reduced by approximately 60% compared to the control group, while cell proliferative capacity was restored after rescuing FUBP3 expression (Fig. 2G). Combined with TUNEL and EdU experimental results, we confirmed that FUBP3 maintains survival advantages in lung cancer cells by promoting cell proliferation and inhibiting cell apoptosis.

3.3 FUBP3 Silencing Suppresses Lung Cancer Metastatic Capacity

To validate the functional role of FUBP3 in lung cancer metastasis *in vivo*, we established a nude mouse tail vein injection metastasis model. Stably transfected A549 cells (Scramble control group, sh-FUBP3 knockdown group, and shRNA-rescue group) were injected into nude mice via tail vein, and mice were sacrificed after 6 weeks to collect lung tissues for pathological analysis. HE staining results showed that compared to the control group, the number and size of pulmonary metastatic foci in the FUBP3 knockdown group were reduced, with metastatic foci exhibiting smaller and more dispersed distribution patterns, while metastatic foci formation capacity was significantly restored after rescuing FUBP3 expression (Fig. 3A). Quantitative analysis results demonstrated that FUBP3 knockdown inhibited the *in vivo* metastatic capacity of lung cancer cells. Control group mice formed approximately 15–20 metastatic foci per lung on average, while the sh-FUBP3 group showed reduced metastatic foci numbers to approximately 5–8, with a metastatic inhibition rate of 60–70%. After rescuing FUBP3 expression, metastatic foci numbers recovered to approximately 12–16, confirming the FUBP3-dependence of the metastatic inhibition effect ($n = 6$, $p < 0.01$) (Fig. 3B). These *in vivo* experimental results were highly consistent with cellular-level migration and invasion experiments, further confirming FUBP3's critical role in promoting lung cancer metastasis. To analyze the molecular characteristics of metastatic foci in depth, we performed immunofluorescence staining analysis on lung metastatic foci tissues. FUBP3 immunofluorescence staining showed that FUBP3 protein expression levels were decreased in metastatic foci of the sh-FUBP3 group, while FUBP3 expression was effectively restored in the rescue group, validating the persistence and effectiveness of *in vivo* knockdown effects (Fig. 3C). Ki-67 immunofluorescence staining was used to evaluate proliferative activity of tumor cells in metastatic foci. Results showed that the proportion of Ki-67 positive cells in metastatic foci of the sh-FUBP3 group was reduced, with proliferation index decreased by approximately 80% compared to the control group, indicating that FUBP3 knockdown not only inhibited metastatic foci formation but also weakened proliferative capacity of tumor cells in metastatic foci. Proliferative activity of metastatic foci was partially restored after rescuing FUBP3 expression (Fig. 3D). STAT3 immunofluorescence staining analysis revealed that in FUBP3 knockdown metastatic foci, STAT3 protein expression levels were correspondingly decreased, with fluorescence intensity reduced compared to the control group. This result suggests that FUBP3 may exert pro-metastatic effects through regulating STAT3 expression or activity, providing important clues for subsequent mechanistic studies (Fig. 3E). CD31 immunofluorescence staining was used to evaluate angiogenesis in metastatic foci. Results showed that microvessel density around metastatic foci in the sh-FUBP3 group was decreased, with CD31-positive vascular structures reduced compared to the control group, indicating that FUBP3 knockdown may limit metastatic foci growth and development through inhibiting angiogenesis. Rescue experiments confirmed the FUBP3-dependence of this angiogenesis inhibition effect (Fig. 3F). *In vivo* metastasis experimental results clearly confirmed FUBP3's critical role in promoting lung cancer metastasis. FUBP3 knockdown not only reduced the number and size of metastatic foci but also inhibited proliferative activity and angiogenic capacity of tumor cells in metastatic foci. Additionally, the synchronized downregulation of STAT3 expression in metastatic foci suggests potential functional association between them, laying important groundwork for further elucidating the mechanistic role of the FUBP3–STAT3 regulatory axis in lung cancer metastasis.

3.4 FUBP3 Drives Lung Cancer Metastasis by Promoting EMT Processes

To further elucidate FUBP3's functional pathways, we performed functional enrichment analysis on genes positively co-expressed with FUBP3. Results showed that genes co-expressed with FUBP3 were enriched in multiple tumor-related functional pathways, including focal adhesion, regulation of actin cytoskeleton, non-small cell lung cancer, pathways in cancer, JAK–STAT signaling pathway, vascular endothelial growth factor (VEGF) signaling pathway, and Extracellular Matrix (ECM)-receptor interaction (Fig. 4A). Enrichment of these pathways further supports FUBP3's important role in regulating cell motility, invasion, and EMT processes, while enrichment of the JAK–STAT signaling pathway suggests that STAT3 may be an important downstream molecule of FUBP3. Cytoskeletal staining showed control A549 and H460 cells exhibited spindle-shaped mesenchymal morphology with pseudopo-

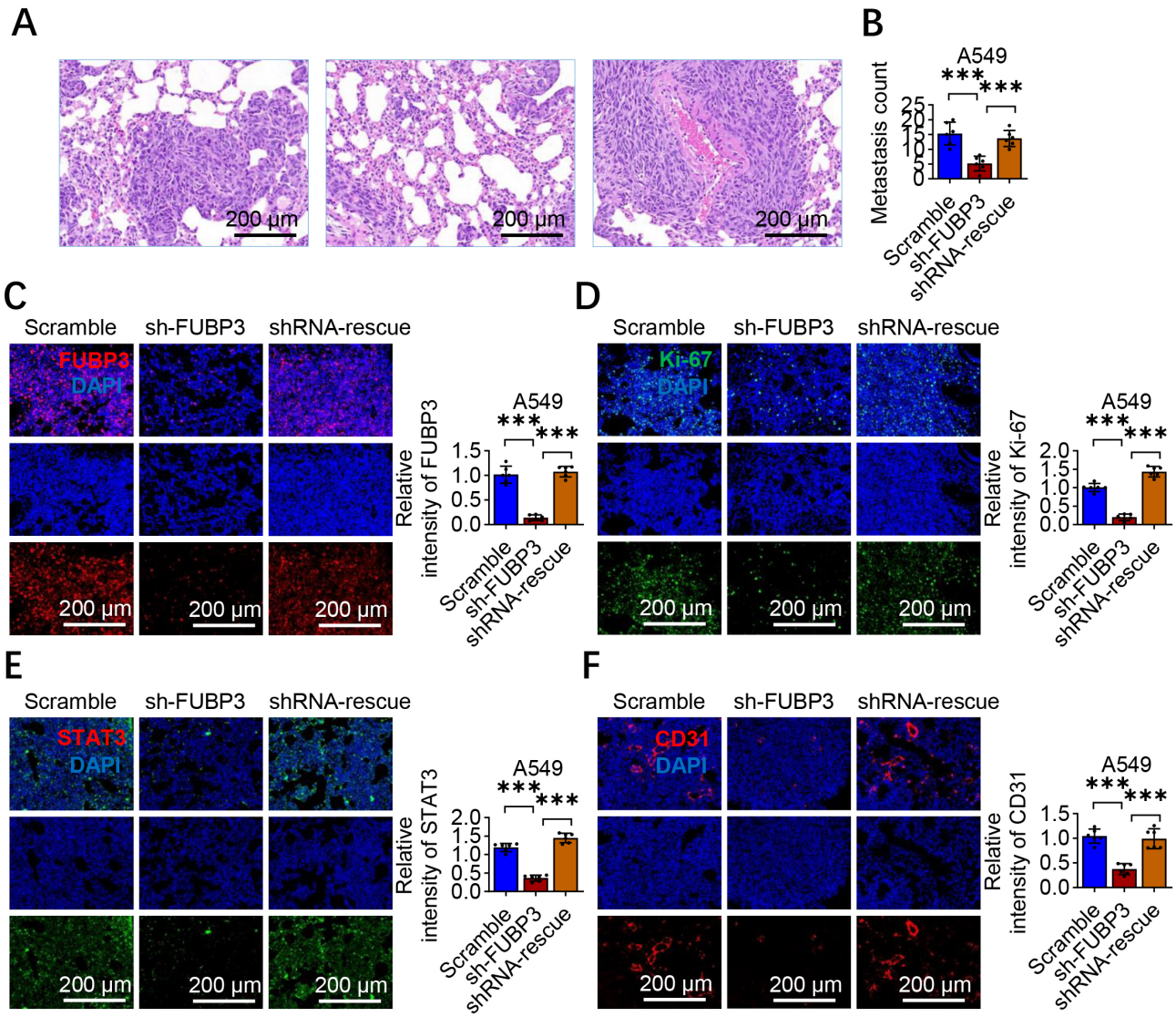

Fig. 3. FUBP3 silencing suppresses lung cancer metastatic capacity *in vivo*. (A) Experimental scheme of tail vein injection metastasis model using A549 cells with FUBP3 modifications. Scale bar: 200 μm. (B) Quantitative analysis of pulmonary metastatic nodules in nude mice (n = 6 per group). (C) Representative immunofluorescence staining of FUBP3 (green) in lung metastatic lesions. DAPI (blue) indicates nuclei. Scale bar: 200 μm. (D) Ki-67 immunofluorescence staining (green) showing proliferation in lung metastatic tissues. Scale bar: 200 μm. (E) STAT3 (green) and (F) CD31 (red) immunofluorescence staining in lung metastatic lesions demonstrating reduced expression in FUBP3 knockdown groups. Scale bar: 200 μm. Data are presented as mean ± SD (n = 6 mice per group). Statistical comparisons were performed using one-way ANOVA followed by Tukey's post hoc test. ***$p < 0.001$.

dia. FUBP3 knockdown induced rounded epithelial-like morphology with tighter intercellular connections, which was reversed upon FUBP3 rescue (Fig. 4B). Scanning electron microscopy confirmed that sh-FUBP3 cells had smoother surfaces with reduced pseudopodia, while control and rescue groups displayed abundant membrane protrusions characteristic of motile cells (Fig. 4C). These morphological changes are highly consistent with characteristics of cellular transformation from epithelial to mesenchymal phenotype during EMT processes. To validate EMT marker changes at the molecular level, we performed immunofluorescence staining analysis. E-cadherin immunofluorescence staining showed that FUBP3 knockdown upregulated expression of the epithelial marker E-cadherin, with E-cadherin primarily localized at cell membranes, forming continuous staining patterns at intercellular junctions. In contrast, E-cadherin expression was relatively low in control and rescue groups, with more dispersed distribution (Fig. 4D). Conversely, immunofluorescence staining of the mesenchymal marker Vimentin showed opposite changes. In control and rescue group cells, Vimentin exhibited typical filamentous distribution in the cytoplasm

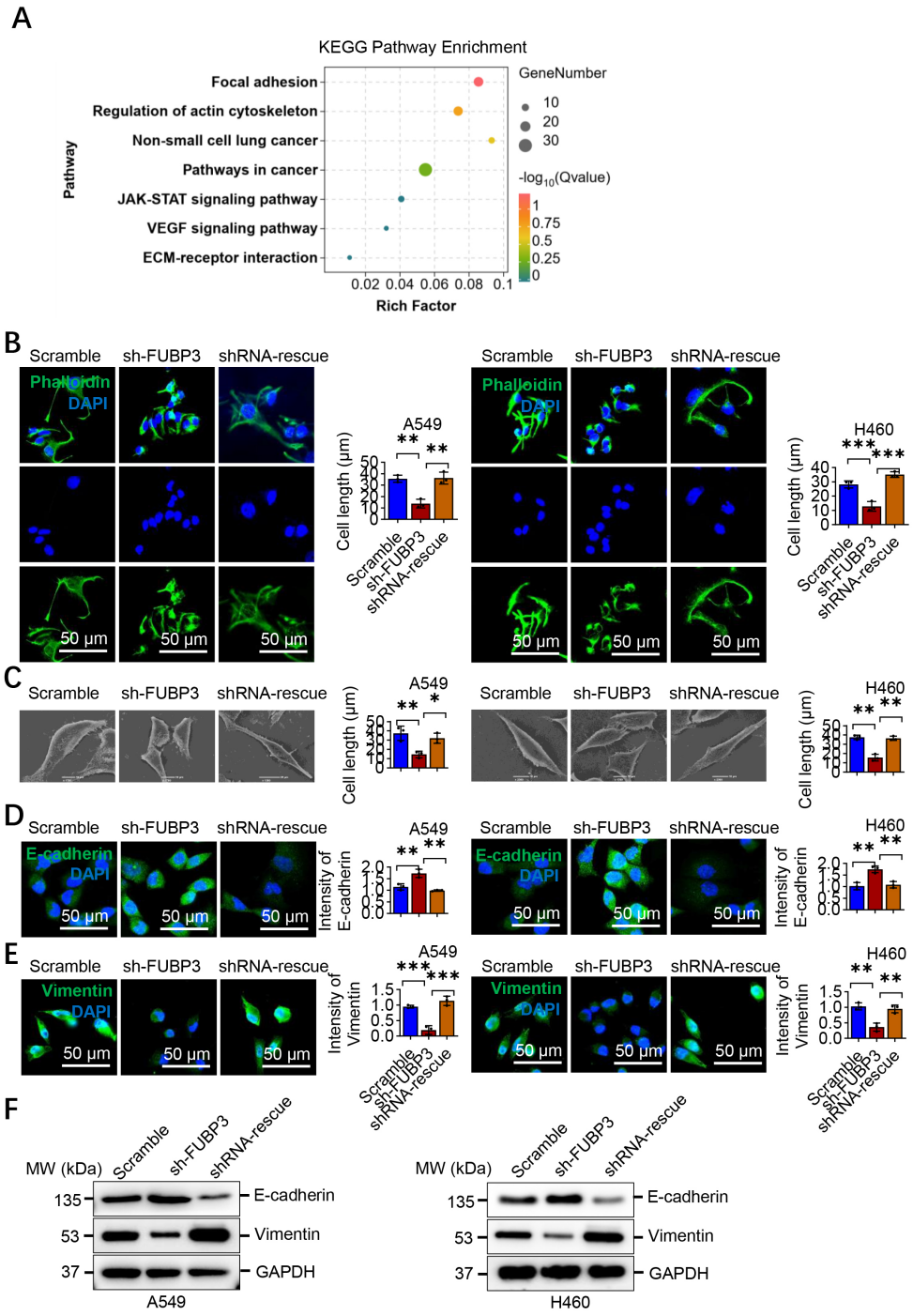

Fig. 4. FUBP3 drives lung cancer metastasis by promoting EMT process. (A) KEGG pathway enrichment analysis of FUBP3 positively co-expressed genes showing significant enrichment in focal adhesion, actin cytoskeleton regulation, JAK–STAT pathway and cancer-related pathways. Analysis was performed using TCGA lung adenocarcinoma dataset. The bubble size represents gene count and color indicates adjusted *p*-value. (B) Phalloidin staining (green) showing cytoskeleton organization in A549 and H460 cells following FUBP3 manipulation. DAPI (blue) indicates nuclei. Scale bar: 50 μm. (C) Scanning electron microscopy analysis revealing morphological changes in A549 and H460 cells with FUBP3 knockdown and rescue. Scale bar: 10 μm. (D) Immunofluorescence staining for epithelial marker E-cadherin (green) in FUBP3-modified A549 and H460 cells. Scale bar: 50 μm. (E) Immunofluorescence analysis of mesenchymal marker Vimentin (red) expression in A549 and H460 cells. Scale bar: 50 μm. (F) Western blot analysis of EMT markers E-cadherin and Vimentin in FUBP3 knockdown and rescue cell lines. Data are presented as mean ± SD from three independent biological replicates (n = 3). Statistical comparisons were performed using one-way ANOVA followed by Tukey's post hoc test. *$p < 0.05$, **$p < 0.01$, ***$p < 0.001$.

with high expression levels. In the sh-FUBP3 group, Vimentin expression was decreased with significantly reduced filamentous structures, indicating weakened cellular mesenchymal characteristics (Fig. 4E). Western blot analysis further quantitatively confirmed EMT marker expression changes. In both A549 and H460 cell lines, FUBP3 knockdown resulted in upregulated E-cadherin protein levels and downregulated Vimentin protein levels. After rescuing FUBP3 expression, E-cadherin expression was downregulated while Vimentin expression was upregulated, reversing the EMT marker expression pattern (Fig. 4F). This result was consistent across two independent lung cancer cell lines, further confirming FUBP3's important role in regulating EMT processes.

3.5 FUBP3 Promotes Lung Cancer Progression by Upregulating Twist1 Expression in Lung Cancer

To further elucidate the molecular mechanisms by which FUBP3 regulates EMT, we examined the effects of FUBP3 on major EMT transcription factors. qRT-PCR analysis showed that FUBP3 knockdown reduced mRNA expression levels of Twist1 and snail family transcriptional repressor 1 (SNALl), while having no effect on Zinc finger E-box-binding homeobox 1 (ZEB1) expression. Among these, Twist1 expression downregulation was most significant, suggesting it may be a key downstream molecule in FUBP3-mediated EMT regulation (Fig. 5A). Immunofluorescence staining further confirmed that FUBP3 knockdown led to reduced Twist1 protein expression in the cell nucleus, with nuclear fluorescence intensity decreased by approximately 70% compared to the control group (Fig. 5B). Clinical sample correlation analysis showed that FUBP3 and Twist1 expression levels were positively correlated in lung cancer patient tissues ($p < 0.01$), further supporting their functional association in lung cancer (Fig. 5C). This clinical evidence provides important support for the role of the FUBP3-Twist1 regulatory axis in lung cancer progression. To establish the functional role of Twist1 in lung cancer progression, we first examined the effects of Twist1 manipulation alone in A549 cells. Twist1 knockdown significantly suppressed malignant phenotypes, including reduced cell length indicating epithelial morphology (**Supplementary Fig. 2A,B**), decreased invasive capacity (**Supplementary Fig. 2C**), and diminished proliferation (**Supplementary Fig. 2D**). Conversely, Twist1 overexpression alone promoted mesenchymal morphology with increased cell length (**Supplementary Fig. 3A,B**), enhanced invasion (**Supplementary Fig. 3C**), and increased proliferation (**Supplementary Fig. 3D**). These results confirm that Twist1 is sufficient and necessary to drive EMT and malignant phenotypes in lung cancer cells, providing a foundation for subsequent rescue experiments. To verify whether Twist1 mediates FUBP3's functional effects, we performed rescue experiments. Overexpression of Twist1 in FUBP3 knockdown A549 cells showed through cytoskeletal staining that FUBP3 knockdown alone caused cells to transition from spindle-shaped mesenchymal-like morphology toward rounded epithelial-like morphology, while Twist1 overexpression effectively reversed this morphological change, enabling cells to regain spindle-shaped mesenchymal-like characteristics (Fig. 5D). Scanning electron microscopy analysis further confirmed this phenomenon, with Twist1 overexpression restoring pseudopodia and membrane protrusion structures on cell surfaces, with cells re-exhibiting motile morphology (Fig. 5E). Functional experiments confirmed that Twist1 can rescue phenotypic defects caused by FUBP3 knockdown. Transwell invasion assays showed that Twist1 overexpression in FUBP3 knockdown cells restored cellular invasive capacity, with invasive cell numbers even exceeding control group levels (Fig. 5F). Clonogenic sphere formation assays demonstrated that Twist1 overexpression could rescue sphere formation capacity defects caused by FUBP3 knockdown, with both sphere number and size restored (Fig. 5G). EdU proliferation assays also showed similar results, with Twist1 overexpression effectively reversing the proliferative capacity decline caused by FUBP3 knockdown (Fig. 5H). *In vivo* metastasis experiments further validated Twist1's critical role in FUBP3 function. In the nude mouse tail vein injection model, FUBP3 knockdown reduced pulmonary metastatic foci formation, while Twist1 overexpression simultaneously with FUBP3 knockdown effectively rescued metastatic capacity, with metastatic foci numbers even exceeding those of the control group (Fig. 5I). This result clearly confirms that Twist1 is a key downstream effector molecule in FUBP3-promoted lung cancer metastasis. To further validate the bidirectionality of the FUBP3-Twist1 regulatory axis, we performed reverse validation experiments. Twist1 was knocked down in FUBP3-overexpressing A549 cells to observe effects on cellular phenotype. Cytoskeletal staining showed that FUBP3 overexpression promoted cellular transformation toward more typical mesenchymal morphology, with cells becoming longer and thinner, while Twist1 knockdown could partially reverse this morphological change (Fig. 5J). Scanning electron microscopy analysis confirmed that Twist1 knockdown weakened the cell surface structural complexity induced by FUBP3 overexpression (Fig. 5K). Functional analysis showed that Twist1 knockdown in FUBP3-overexpressing cells inhibited cellular invasive capacity (Fig. 5L), sphere formation capacity (Fig. 5M), and proliferative capacity (Fig. 5N), indicating that Twist1 deficiency can block FUBP3's pro-oncogenic functions. *In vivo* metastasis experiments confirmed that Twist1 knockdown can inhibit the metastasis-promoting effects induced by FUBP3 overexpression, with metastatic foci numbers reduced by approximately 70% compared to the FUBP3 overexpression group (Fig. 5O).

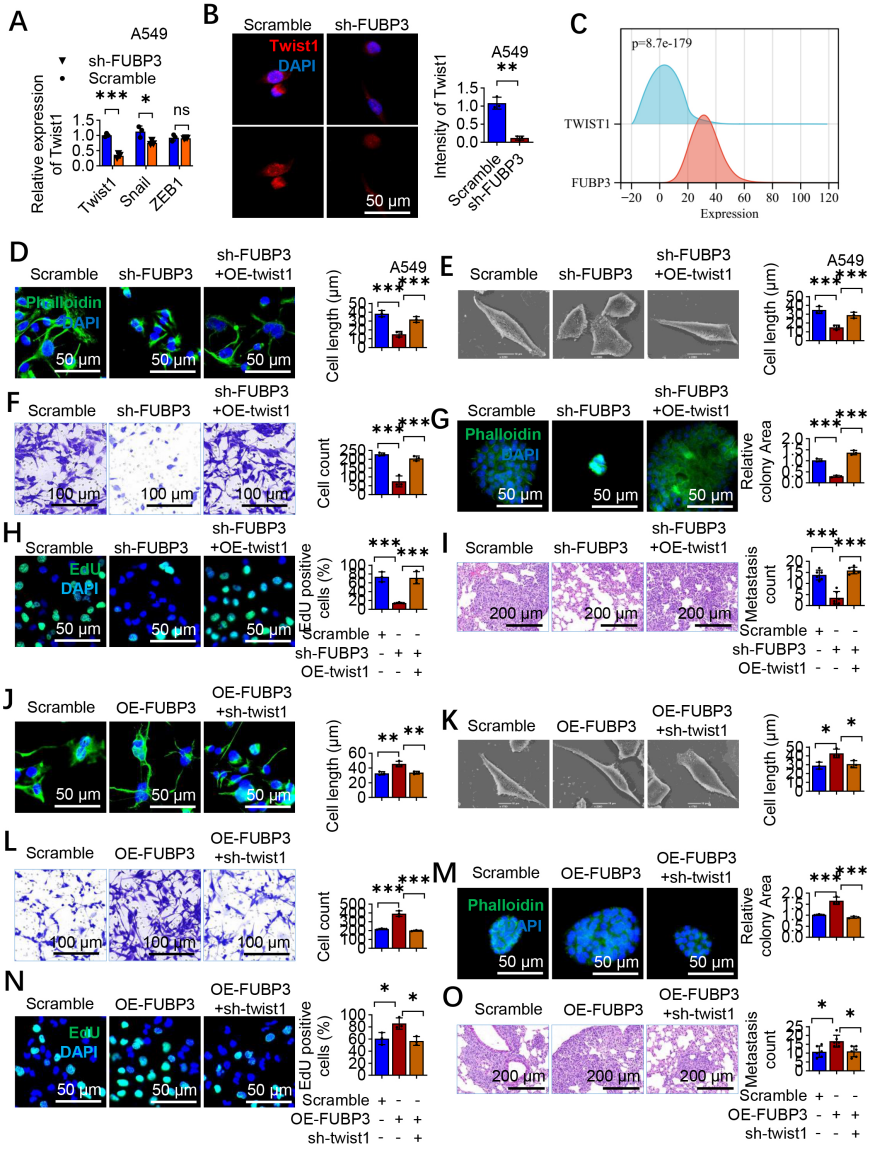

Fig. 5. FUBP3 promotes lung cancer progression through upregulation of Twist1 expression. (A) qRT-PCR analysis of EMT transcription factors in FUBP3 knockdown A549 cells showing significant reduction in Twist1 expression. Gene expression was normalized to GAPDH. (B) Immunofluorescence staining confirming reduced Twist1 protein (green) in FUBP3 knockdown A549 cells. Representative images (left) and quantification of fluorescence intensity (right) are shown. DAPI (blue) indicates nuclei. Scale bar: 50 μm. (C) Correlation analysis showing positive association between FUBP3 and Twist1 expression in lung cancer patients ($p = 8.7 \times 10^{-179}$). (D) Phalloidin staining demonstrating morphological rescue by Twist1 overexpression in FUBP3 knockdown A549 cells. Scale bar: 50 μm. (E) SEM analysis showing reversal of epithelial morphology by Twist1 overexpression in FUBP3-silenced cells. Scale bar: 10 μm. (F) Transwell invasion assay with FUBP3 knockdown and Twist1 rescue in A549 cells. Scale bar: 100 μm. (G) Sphere formation assay evaluating rescue effects of Twist1 overexpression. Scale bar: 200 μm. (H) EdU proliferation assay showing functional rescue by Twist1. Scale bar: 50 μm. (I) *In vivo* metastasis analysis using A549 cells with FUBP3 knockdown and Twist1 rescue. Scale bar: 200 μm. (J,K) Morphological analysis showing FUBP3 overexpression-induced mesenchymal transition reversed by Twist1 silencing using phalloidin staining (J) and SEM (K). Scale bar: 50 μm. (L) Invasion assay with FUBP3 overexpression and Twist1 knockdown. (M) Sphere formation analysis with combined treatments. Scale bar: 200 μm. (N) EdU proliferation assay in cells with FUBP3 overexpression and Twist1 silencing. Scale bar: 50 μm. (O) *In vivo* metastasis assessment with A549 cells harboring FUBP3 overexpression and Twist1 knockdown. Scale bar: 200 μm. Data are presented as mean ± SD from three independent biological replicates (n = 3 for *in vitro* experiments, n = 6 mice per group for *in vivo* experiments). Statistical comparisons were performed using one-way ANOVA followed by Tukey's post hoc test. ns, not significant, *$p < 0.05$, **$p < 0.01$, ***$p < 0.001$.

3.6 FUBP3-STAT3 Interaction Upregulates Twist1 to Promote Lung Cancer Progression

To explore the molecular mechanisms by which FUBP3 regulates Twist1, based on the enrichment of JAK–STAT signaling pathway in previous functional enrichment analysis, we focused on investigating the potential interaction between FUBP3 and STAT3. Protein–protein interaction network analysis revealed a direct protein interaction relationship between FUBP3 and STAT3, suggesting they may form functional complexes to co-regulate downstream gene expression (Fig. 6A). Clinical sample analysis showed that FUBP3 and STAT3 expression levels were positively correlated in lung cancer tissues ($p < 0.01$), and this strong correlation suggests potential synergistic effects between them in lung cancer development and progression (Fig. 6B). To verify the intracellular interaction between FUBP3 and STAT3, we performed immunofluorescence co-staining experiments. Results showed that FUBP3 and STAT3 exhibited distinct co-localization patterns in A549 cells, indicating high spatial overlap of the two proteins (Fig. 6C). To further validate the direct physical interaction between FUBP3 and STAT3 *in situ*, we performed PLA in A549 cells. The PLA results showed abundant red fluorescent signals representing FUBP3–STAT3 interaction within 40 nm proximity (Fig. 6D). Additionally, we assessed the interactions in FUBP3-knockdown cells using a PLA to provide complementary evidence of this interaction. The PLA results indicated a significant reduction of positive signals in FUBP3-silenced cells compared to control cells, further supporting the relationship between FUBP3 and STAT3 in lung cancer progression. Using anti-FUBP3 antibody for immunoprecipitation, Western blot detection showed co-precipitation of STAT3 protein, while the IgG negative control group showed no detectable STAT3 signal. Reverse Co-IP experiments using anti-STAT3 antibody for immunoprecipitation similarly co-precipitated FUBP3 protein (Fig. 6E). This bidirectional Co-IP result clearly confirms that FUBP3 and STAT3 form stable protein complexes within cells. Input represents 5% of total lysate. Note that no bands were detected in IgG control lanes, confirming the specificity of the interaction. To validate the functional importance of STAT3 in lung cancer progression, we first examined the effects of STAT3 knockdown alone in A549 cells. STAT3 knockdown significantly suppressed malignant phenotypes, including altered cell morphology with reduced cell length (**Supplementary Fig. 4A,B**), decreased invasive capacity (**Supplementary Fig. 4C**), and diminished proliferation (**Supplementary Fig. 4D**). To verify whether STAT3 mediates FUBP3's regulatory effect on Twist1, we knocked down STAT3 in FUBP3-overexpressing A549 cells. Immunofluorescence staining showed that FUBP3 overexpression upregulated Twist1 expression in the cell nucleus, with nuclear fluorescence intensity increased approximately 1.5-fold compared to the control group. However, after STAT3 knockdown, Twist1 expression levels decreased, nearly returning to control group levels, indicating that STAT3 is necessary for FUBP3-mediated Twist1 upregulation (Fig. 6F). Cell morphological analysis showed that FUBP3 overexpression promoted A549 cell transformation toward typical spindle-shaped mesenchymal-like morphology, with cells becoming longer and thinner and pseudopodial structures more prominent. However, STAT3 knockdown effectively reversed this morphological change, with cells re-exhibiting relatively rounded morphology and significantly weakened mesenchymal characteristics (Fig. 6G). This result indicates that STAT3 is a key molecule in FUBP3-mediated regulation of cellular EMT morphological transformation. Functional experiments further confirmed STAT3's necessity in FUBP3 function. Transwell invasion assays showed that FUBP3 overexpression enhanced cellular invasive capacity, with invasive cell numbers increased approximately 2-fold compared to the control group. However, STAT3 knockdown suppressed this pro-invasive effect, with invasive cell numbers reduced to near control group levels (Fig. 6H). Clonogenic sphere formation assays showed similar result patterns. FUBP3 overexpression promoted sphere formation, with both sphere number and size significantly increased, while STAT3 knockdown effectively reversed this promoting effect, with sphere formation capacity returning to control group levels (Fig. 6I). EdU proliferation assays also confirmed that STAT3 knockdown could block the enhanced cell proliferative capacity induced by FUBP3 overexpression, with the proportion of EdU-positive cells reduced to control group levels (Fig. 6J). Most importantly, *in vivo* metastasis experiments confirmed STAT3's critical role in FUBP3's pro-metastatic function. In the nude mouse tail vein injection model, FUBP3 overexpression increased the number and size of pulmonary metastatic foci, with metastatic foci numbers increased approximately 2-fold compared to the control group. However, after STAT3 knockdown, the metastasis-promoting effect was suppressed, with metastatic foci numbers reduced to near control group levels (Fig. 6K). This *in vivo* experimental result clearly confirms that STAT3 is an indispensable molecular partner for FUBP3 to exert its pro-metastatic function.

3.7 STAT3 Inhibitor (S3I-201) Treatment Reverses the Promoting Effects of Elevated FUBP3 Expression in Lung Cancer Cells

To further validate STAT3's critical role in FUBP3-mediated regulation of lung cancer metastasis and explore potential therapeutic targets, we treated FUBP3-overexpressing A549 cells with the STAT3 small molecule inhibitor S3I-201 and systematically evaluated its antagonistic effects on FUBP3 function. Twist1 immunofluorescence staining analysis showed that FUBP3 overexpression upregulated Twist1 expression in the cell nucleus, with nuclear fluorescence intensity increased ap-

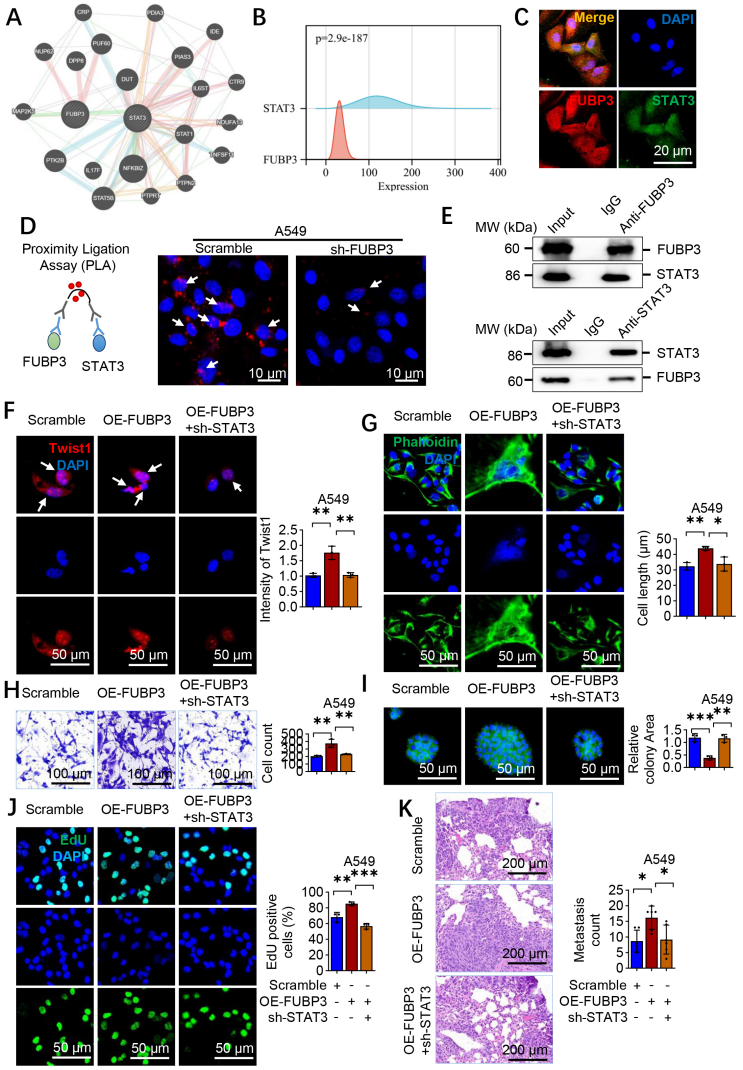

Fig. 6. FUBP3–STAT3 interaction upregulates Twist1 to promote lung cancer progression. (A) Protein–protein interaction network analysis revealing direct interaction between FUBP3 and STAT3. (B) Positive correlation between FUBP3 and STAT3 expression in lung cancer datasets ($p = 2.9 \times 10^{-187}$). (C) Immunofluorescence co-localization of FUBP3 (green) and STAT3 (red) in A549 cells. Merge panel shows co-localization (yellow). Scale bar: 20 μm. (D) Proximity ligation assay (PLA) demonstrating direct interaction between FUBP3 and STAT3 in scramble and shFUBP3 A549 cells. Red fluorescent dots indicate protein–protein interaction within 40 nm proximity. DAPI (blue) indicates nuclei. Scale bar: 10 μm. The PLA results indicate a significant interaction between FUBP3 and STAT3, which supports their role in regulating lung cancer progression. In FUBP3-knockdown cells, a notable reduction in positive PLA signals was observed, further indicating the importance of FUBP3 in this interaction. White arrows indicate fluorescent spots in interaction regions. (E) FUBP3 physically interacts with STAT3 in lung cancer cells. Co-immunoprecipitation assays were performed using Input (whole cell lysate), IgG (beads plus nonspecific antibody) serving as negative control and experimental Groups (with Anti-FUBP3 or Anti-STAT3 antibodies). (F) Immunofluorescence analysis of Twist1 (green) showing FUBP3 overexpression-induced upregulation reversed by STAT3 silencing. White arrows indicate positive nuclear expression of Twist1. Scale bar: 50 μm. (G) Phalloidin staining revealing mesenchymal morphology induced by FUBP3 overexpression and its reversal by STAT3 knockdown. Scale bar: 50 μm. (H) Transwell invasion assay with FUBP3 overexpression and STAT3 silencing in A549 cells. Scale bar: 100 μm. (I) Sphere formation analysis showing rescue effects of STAT3 knockdown. Scale bar: 200 μm. (J) EdU proliferation assay demonstrating functional rescue by STAT3 silencing. Scale bar: 50 μm. (K) *In vivo* metastasis analysis with A549 cells harboring FUBP3 overexpression and STAT3 knockdown modifications. Scale bar: 200 μm. Data are presented as mean ± SD from three independent biological replicates (n = 3 for *in vitro* experiments, n = 6 mice per group for *in vivo* experiments). Statistical comparisons were performed using one-way ANOVA followed by Tukey's post hoc test. $*p < 0.05$, $**p < 0.01$, $***p < 0.001$. "+" indicates the presence of a treatment, while "–" indicates the absence of a treatment.

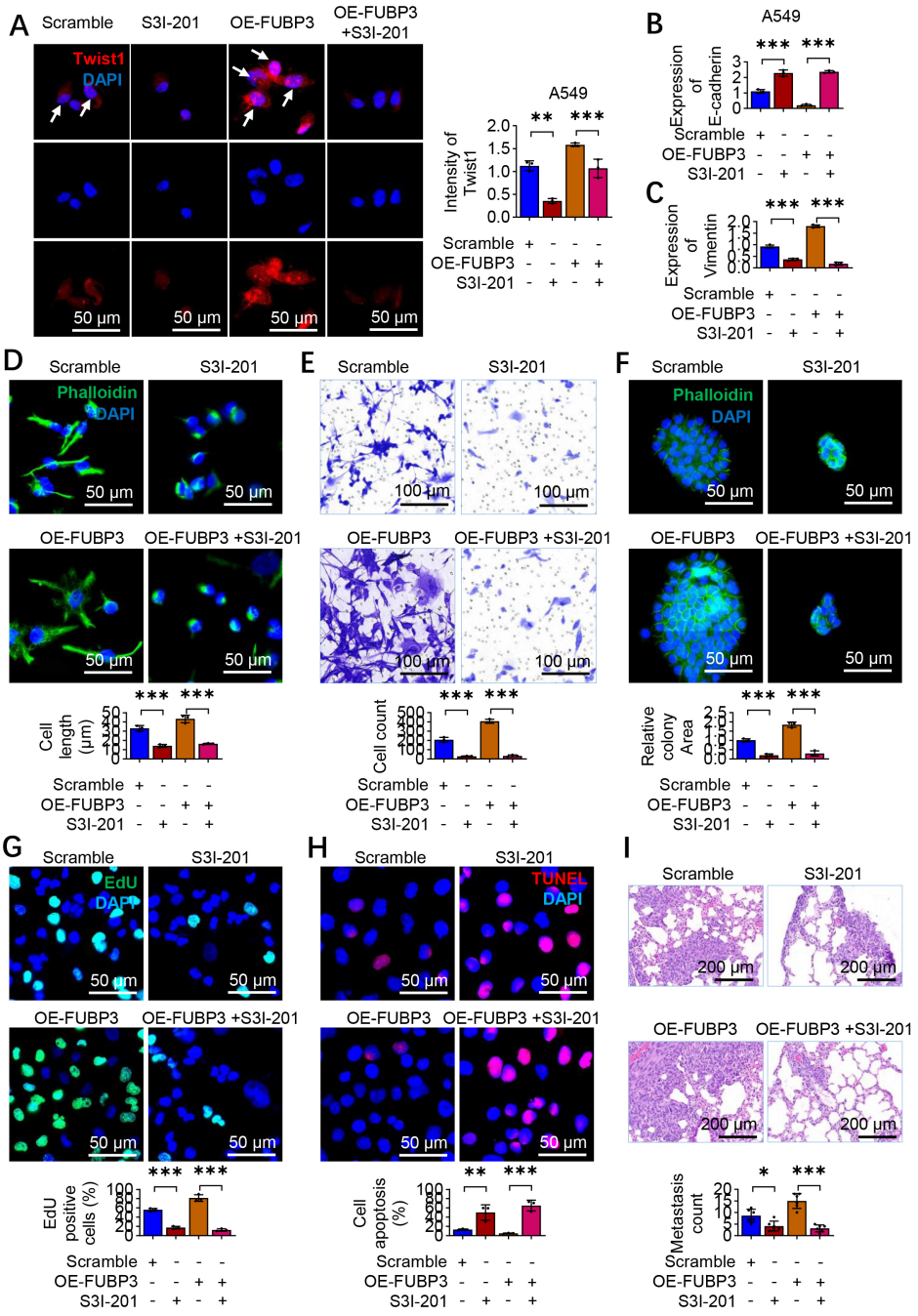

Fig. 7. STAT3 inhibitor S3I-201 reverses FUBP3-induced lung cancer progression. (A) Immunofluorescence staining showing Twist1 (green) expression in A549 cells treated with FUBP3 overexpression and STAT3 inhibitor S3I-201. White arrows indicate positive nuclear expression of Twist1. Scale bar: 50 μm. (B,C) PCR analysis of epithelial marker E-cadherin (B) and mesenchymal marker Vimentin (C) in A549 cells with FUBP3 overexpression and S3I-201 treatment. (D) Phalloidin staining demonstrating morphological changes in A549 cells with FUBP3 overexpression and S3I-201 treatment. Scale bar: 50 μm. (E) Transwell invasion assay evaluating the effects of S3I-201 on FUBP3-overexpressing cells. Scale bar: 100 μm. (F) Sphere formation assay with FUBP3 overexpression and S3I-201 treatment. Scale bar: 50 μm. (G) EdU proliferation assay with FUBP3 overexpression and S3I-201 treatment. Scale bar: 50 μm. (H) TUNEL assay assay with FUBP3 overexpression and S3I-201 treatment. Scale bar: 50 μm. (I) *In vivo* metastasis analysis with S3I-201 treatment in FUBP3-overexpressing A549 cells. Scale bar: 200 μm. Data are presented as mean ± SD from three independent biological replicates (n = 3 for *in vitro* experiments, n = 6 mice per group for *in vivo* experiments). Statistical comparisons were performed using one-way ANOVA followed by Tukey's post hoc test. *$p < 0.05$, **$p < 0.01$, ***$p < 0.001$. "+" indicates the presence of a treatment, while "−" indicates the absence of a treatment.

proximately 1.5-fold compared to the control group. S3I-201 treatment alone reduced basal Twist1 expression levels. Importantly, S3I-201 effectively reversed the Twist1 upregulation induced by FUBP3 overexpression, reducing its expression levels (Fig. 7A). This result confirms the necessity of STAT3 activity for FUBP3-mediated Twist1 regulation. To comprehensively evaluate S3I-201's effects on EMT markers, we examined transcriptional level changes in epithelial and mesenchymal markers. qRT-PCR analysis showed that S3I-201 treatment upregulated mRNA expression of the epithelial marker E-cadherin, while FUBP3 overexpression reduced E-cadherin expression. S3I-201 effectively reversed the E-cadherin downregulation induced by FUBP3 overexpression (Fig. 7B). Conversely, expression changes of the mesenchymal marker Vimentin showed opposite trends: S3I-201 treatment reduced basal Vimentin expression, while FUBP3 overexpression upregulated Vimentin expression, and S3I-201 effectively blocked this upregulation effect (Fig. 7C). Cell morphological analysis confirmed S3I-201's antagonistic effects on EMT processes. Cytoskeletal staining showed that FUBP3 overexpression promoted A549 cell transformation toward typical spindle-shaped mesenchymal-like morphology, with cells becoming longer and thinner. Addition of S3I-201 to FUBP3-overexpressing cells effectively reversed mesenchymal-like morphological changes, with cells re-exhibiting relatively rounded and tightly connected epithelial-like characteristics (Fig. 7D). Functional experiments further confirmed S3I-201's antagonistic effects on FUBP3's pro-oncogenic functions. Transwell invasion assays showed that S3I-201 treatment inhibited basal cellular invasive capacity, while FUBP3 overexpression enhanced invasive capacity. Importantly, S3I-201 effectively reversed the invasion-promoting effects induced by FUBP3 overexpression, reducing invasive cell numbers (Fig. 7E). Clonogenic sphere formation assays showed similar result patterns. S3I-201 treatment inhibited cellular sphere formation capacity, while FUBP3 overexpression promoted sphere formation. S3I-201 effectively blocked the promoting effects of FUBP3 overexpression, with both sphere number and size reduced (Fig. 7F). EdU proliferation assays confirmed that S3I-201 not only inhibited basal cellular proliferative activity but also completely reversed the proliferation-promoting effects induced by FUBP3 overexpression (Fig. 7G). TUNEL apoptosis assays showed that S3I-201 treatment increased cellular apoptosis levels, with the proportion of TUNEL-positive cells increased approximately 2–3-fold compared to the control group. FUBP3 overexpression reduced basal cellular apoptosis levels, while S3I-201 reversed this anti-apoptotic effect, restoring apoptosis levels to or even exceeding control group levels (Fig. 7H). This result indicates that STAT3 activity is necessary for FUBP3's anti-apoptotic function. Most importantly, *in vivo* metastasis experiments confirmed S3I-201's therapeutic potential. In the nude mouse tail vein injection model, S3I-201 treatment reduced pulmonary metastatic foci formation. FUBP3 overexpression increased metastatic foci numbers, while S3I-201 effectively reversed this pro-metastatic effect, reducing metastatic foci numbers to below control group levels (Fig. 7I). This *in vivo* experimental result provides important pharmacodynamic evidence for S3I-201 as a potential therapeutic agent. In summary, the STAT3 small molecule inhibitor S3I-201 comprehensively antagonizes FUBP3's pro-oncogenic functions by inhibiting STAT3 activity to block the FUBP3-STAT3-Twist1 regulatory axis, reversing EMT processes, inhibiting cell proliferation, invasion, and metastatic capacity, and promoting cell apoptosis. These results not only further confirm STAT3's central role in FUBP3 function but also provide important experimental evidence for STAT3 inhibition-based lung cancer therapeutic strategies. The effective antagonistic effects of S3I-201 indicate that targeting the FUBP3-STAT3 regulatory axis may become a novel strategy for precision lung cancer therapy (Fig. 8).

4. Discussion

This research highlights the significant function of FUBP3 in lung cancer metastasis via a newly identified FUBP3-STAT3-Twist1 regulatory axis that facilitates the EMT. Our findings indicate that FUBP3 physically interacts with STAT3 to enhance Twist1 transcription, resulting in cytoskeletal remodeling, downregulation of E-cadherin, and upregulation of vimentin, which ultimately facilitates cancer cell invasion and metastasis. Pharmacological inhibition of STAT3 with S3I-201 effectively reverses metastatic phenotypes induced by FUBP3. The findings offer mechanistic insights into lung cancer metastasis and identify FUBP3 as a potential therapeutic target for clinical intervention.

FUBP3, a member of the RBP family, has seen relatively delayed functional studies in tumors [23,24,34]. This study demonstrates that FUBP3 upregulation in lung cancer correlates with poor patient prognosis, aligning with existing research indicating that its family member, FUBP1 plays an oncogenic role in multiple tumors. Bioinformatics analysis indicates that lung cancer patients exhibiting elevated FUBP3 expression experience reduced OS. Furthermore, FUBP3 expression levels in M1 stage patients are significantly greater than those in M0 stage patients, implying a direct correlation between FUBP3 and the metastatic potential of lung cancer. This clinical association establishes a significant pathological basis for future functional studies and indicates that FUBP3 may function as a potential biomarker for prognostic evaluation in lung cancer. Functional experiments provide additional evidence for the role of FUBP3 in promoting lung cancer metastasis. Silencing FUBP3 expression via RNA interference technology resulted in decreased migration and invasion capabilities of lung cancer cells. This finding was corroborated

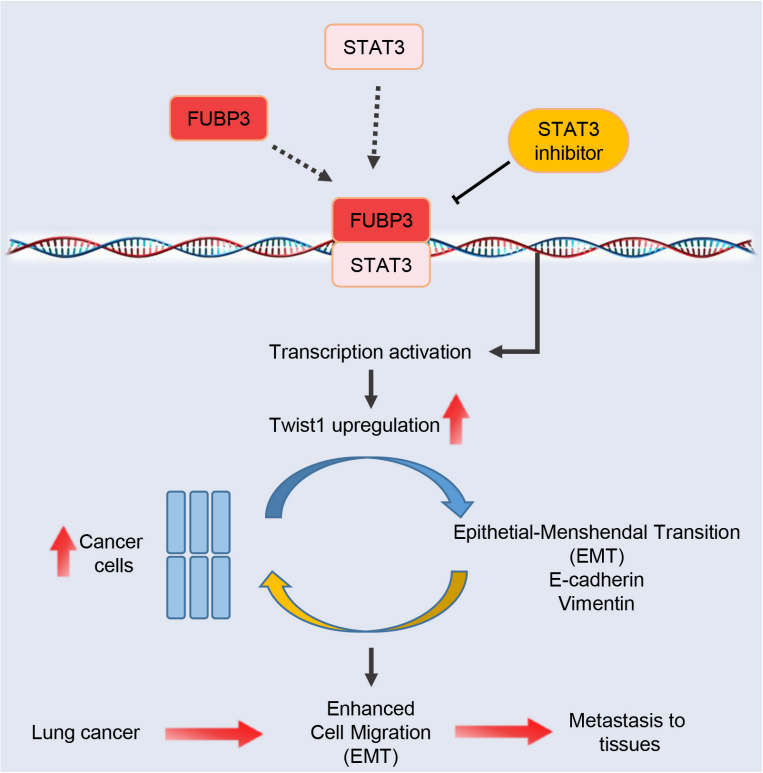

Fig. 8. Proposed mechanistic model. Schematic illustration of the FUBP3-STAT3-Twist1 regulatory axis promoting epithelial-mesenchymal transition (EMT) and lung cancer metastasis. FUBP3 physically interacts with STAT3 to enhance Twist1 transcription, leading to downregulation of epithelial marker E-cadherin and upregulation of mesenchymal marker Vimentin, accompanied by actin cytoskeleton remodeling. This cascade ultimately drives EMT process, enhancing cancer cell migration, invasion, self-renewal capacity, and metastatic potential.

across multiple lung cancer cell lines, suggesting a universal regulatory role of FUBP3 in lung cancer metastasis. *In vivo* metastasis experiments indicate that FUBP3 knockdown leads to a reduction in pulmonary metastatic foci formation, thereby confirming the critical regulatory role of FUBP3 in lung cancer metastasis in the *in vivo* context. The findings correspond with contemporary research trends concerning the functions of RBPs in tumor metastasis, underscoring their significant role as regulatory factors in this process.

The EMT process is a critical step for tumors to acquire metastatic capacity [35–37], and our study confirms that FUBP3 promotes lung cancer metastasis through regulating the EMT process. After the knockdown of FUBP3, epithelial marker E-cadherin expression was upregulated, mesenchymal marker vimentin expression was downregulated, and cellular morphology shifted toward epithelial characteristics. The observed changes suggest that FUBP3 is an important regulatory factor in the EMT. Further analysis indicates that FUBP3 knockdown results in the enrichment of EMT-related gene sets, encompassing various metastasis-associated biological processes such as cytoskeletal remodeling and interactions with extracellular matrix receptors. This finding establishes a direct connection between FUBP3 and EMT, a fundamental mechanism underlying tumor metastasis, thereby offering significant insights into the molecular framework of FUBP3-induced metastasis. FUBP3 knockdown resulted in modest apoptosis and impaired cell proliferation, which may partially explain the observed effects on migration, invasion, and metastasis. The considerable decrease in metastatic capacity observed across multiple functional assays seems to exceed what would be expected from altered cell survival alone, suggesting that FUBP3 coordinately regulates multiple cancer hallmarks, including cell survival and metastatic behavior. Future research utilizing anoikis-resistant cell models or apoptosis inhibitors may elucidate the distinct roles of FUBP3 in cell survival and metastatic potential.

Twist1, as a core transcription factor in the EMT process, has been a research hotspot regarding its regulatory mechanisms [6,38,39]. Our findings indicate that FUBP3 enhances lung cancer progression through the upregulation of Twist1 expression, thereby uncovering a novel mechanism of Twist1 transcriptional regulation. Correlation analysis indicates a positive correlation between FUBP3 and Twist1 expression in lung cancer patient tissues, thereby confirming their functional association in clinical samples. Rescue experiments provide additional evidence that re-

expression of Twist1 can partially counteract the inhibitory effect of FUBP3 knockdown on cellular metastatic capacity, suggesting that Twist1 serves as a significant downstream target for FUBP3's pro-metastatic function. This finding clarifies the mechanism of FUBP3 action and introduces a new regulatory factor to the upstream regulatory network of Twist1.

Immunofluorescence co-localization and co-immunoprecipitation experiments validated the direct interaction between FUBP3 and STAT3, establishing a molecular foundation for the formation of transcriptional complexes. STAT3, an important transcription factor, demonstrates sustained activation in tumors and is associated with multiple malignant phenotypes. This protein–protein interaction pattern is prevalent in transcriptional regulation and signifies a novel application in the regulation of EMT transcription factors. Silencing of STAT3 can counteract the pro-metastatic effects associated with FUBP3 overexpression in lung cancer metastasis, thereby reinforcing the essential role of STAT3 in the metastatic regulation mediated by FUBP3. Treatment experiments utilizing the STAT3 inhibitor S3I-201 yield significant evidence for the clinical applicability of the findings from this study. The S3I-201 treatment has the capacity to reverse the pro-metastatic phenotype observed in cells with high FUBP3 expression and to restore the typical expression patterns of EMT markers. This finding confirms the essential function of STAT3 within the FUBP3–Twist1 regulatory axis and indicates that targeting STAT3 could be a viable approach for treating lung cancers with high FUBP3 expression. *In vivo* experiments indicate that S3I-201 treatment decreases the formation of pulmonary metastatic foci, thereby offering proof-of-concept for precision therapy targeting the FUBP3–STAT3–Twist1 axis.

This study establishes the FUBP3–STAT3–Twist1 regulatory axis, offering a new theoretical framework for comprehending the mechanisms of lung cancer metastasis. This regulatory axis encompasses the roles of RBPs, signal transduction molecules, and transcription factors, highlighting the intricate and multifaceted aspects of gene expression regulation. This regulatory pattern elucidates the pro-metastatic function of FUBP3 and serves as a reference model for exploring the mechanistic roles of other RBPs in tumor metastasis. The findings of this study hold significant translational value from a clinical perspective. FUBP3 expression levels may function as biomarkers for prognostic evaluation in lung cancer patients, aiding in the identification of individuals at elevated metastatic risk. The interaction between FUBP3 and STAT3 presents new targets for drug development. Designing specific inhibitors to disrupt these protein–protein interactions may facilitate precision intervention in metastatic processes. The effectiveness of STAT3 inhibitors reinforces the viability of this therapeutic approach. Our findings indicate that FUBP3 physically interacts with STAT3 and is essential for STAT3-mediated upregulation of Twist1 and EMT in NSCLC. The exact molecular mechanism by which FUBP3 facilitates STAT3-dependent transcriptional regulation necessitates additional research. However, our findings align with growing evidence indicating that STAT3 modulates various transcription factors implicated in cancer metastasis. Prior research indicates that STAT3 activation enhances Twist1 expression across multiple cancer types [40–43]. Furthermore, STAT3 has been shown to influence EMT-related transcription factors via direct DNA binding as well as indirect mechanisms involving protein–protein interactions and transcriptional co-regulation [44–46]. The physical interaction between FUBP3 and STAT3, as demonstrated by Co-IP and PLA experiments, and the functional dependence of Twist1 expression on both proteins indicate that FUBP3 act as a critical co-factor that enhances the transcriptional activity of STAT3. The mechanisms by which this occurs, whether through direct recruitment to the Twist1 promoter, stabilization of STAT3 transcriptional complexes, or modulation of chromatin accessibility, should be further investigated. Our data identify FUBP3 as a new regulator of the STAT3–Twist1 axis, laying the groundwork for comprehending FUBP3's involvement in the promotion of NSCLC metastasis.

This study has several limitations. First, the binding pattern and specific regulatory mechanisms of the FUBP3–STAT3 complex on the Twist1 promoter were not comprehensively examined. Second, the consistent functionality of this regulatory axis across various lung cancer subtypes should be validated. Additionally, apart from Twist1, the FUBP3–STAT3 complex may regulate other genes associated with EMT. Comprehensive screening and functional validation of these potential targets will be crucial for future research.

5. Conclusion

This study elucidates the critical role of FUBP3 in lung cancer metastasis and its underlying molecular mechanisms. Our findings indicate that FUBP3 is highly expressed in lung cancer tissues and is closely associated with poor patient prognosis. Functional studies confirm that FUBP3 enhances the migration and invasion capabilities of lung cancer cells by facilitating EMT processes. Mechanistic investigations indicate that FUBP3 drives lung cancer EMT and metastasis by recruiting STAT3, leading to the formation of transcriptional complexes that specifically activate the expression of the key EMT transcription factor Twist1. The STAT3 inhibitor S3I-201 effectively reverses the pro-metastatic effects mediated by FUBP3, offering evidence for targeted therapeutic approaches. This study establishes the FUBP3–STAT3–Twist1 regulatory axis, offering a novel theoretical framework for elucidating the molecular mechanisms underlying lung cancer metastasis and enhancing the functional understanding of RBPs in tumor

metastasis. FUBP3 may function as a biomarker for prognostic evaluation in lung cancer, and its interaction with STAT3 presents new avenues for drug development.

Availability of Data and Materials

The datasets used and analyzed during the current study are available from the corresponding author on reasonable request.

Author Contributions

WW, LZ and PW designed the study. WW and LZ performed the experiments and analyzed the data. WW and PW wrote the initial draft of the paper, with contributions from all authors. All authors contributed to editorial changes in the manuscript. All authors read and approved the final manuscript. All authors have participated sufficiently in the work and agreed to be accountable for all aspects of the work.

Ethics Approval and Consent to Participate

The animal experiments met the ethical requirements and were approved by the Institutional Animal Care and Use Committee of Liaocheng People's Hospital (approval number: 2025257). We confirm that all animal experiments reported in the manuscript were conducted in accordance with the ARRIVE guidelines. The clinical study was approved by the Medical Ethics Committee of Liaocheng People's Hospital (approval number: 2025256). All procedures were conducted in accordance with the ethical standards of the Declaration of Helsinki, and written informed consent was obtained from all participants.

Acknowledgment

Not applicable.

Funding

This research received no external funding.

Conflict of Interest

The authors declare no conflict of interest.

Supplementary Material

Supplementary material associated with this article can be found, in the online version, at https://doi.org/10.31083/FBL47541.

References

[1] Menju T, Date H. Lung cancer and epithelial-mesenchymal transition. General Thoracic and Cardiovascular Surgery. 2021; 69: 781–789. https://doi.org/10.1007/s11748-021-01595-4.

[2] Lei X, Li Z, Zhong Y, Li S, Chen J, Ke Y, *et al*. Gli1 promotes epithelial-mesenchymal transition and metastasis of non-small cell lung carcinoma by regulating snail transcriptional activity and stability. Acta Pharmaceutica Sinica. B. 2022; 12: 3877–3890. https://doi.org/10.1016/j.apsb.2022.05.024.

[3] Chen B, Song Y, Zhan Y, Zhou S, Ke J, Ao W, *et al*. Fangchinoline inhibits non-small cell lung cancer metastasis by reversing epithelial-mesenchymal transition and suppressing the cytosolic ROS-related Akt-mTOR signaling pathway. Cancer Letters. 2022; 543: 215783. https://doi.org/10.1016/j.canlet.2022.215783.

[4] Nam MW, Kim CW, Choi KC. Epithelial-Mesenchymal Transition-Inducing Factors Involved in the Progression of Lung Cancers. Biomolecules & Therapeutics. 2022; 30: 213–220. https://doi.org/10.4062/biomolther.2021.178.

[5] Kumar V, Yochum ZA, Devadassan P, Huang EHB, Miller E, Baruwal R, *et al*. TWIST1 is a critical downstream target of the HGF/MET pathway and is required for MET driven acquired resistance in oncogene driven lung cancer. Oncogene. 2024; 43: 1431–1444. https://doi.org/10.1038/s41388-024-02987-5.

[6] Yu X, He T, Tong Z, Liao L, Huang S, Fakhouri WD, *et al*. Molecular mechanisms of TWIST1-regulated transcription in EMT and cancer metastasis. EMBO Reports. 2023; 24: e56902. https://doi.org/10.15252/embr.202356902.

[7] Lee Y, Yoon J, Ko D, Yu M, Lee S, Kim S. TMPRSS4 promotes cancer stem-like properties in prostate cancer cells through upregulation of SOX2 by SLUG and TWIST1. Journal of Experimental & Clinical Cancer Research: CR. 2021; 40: 372. https://doi.org/10.1186/s13046-021-02147-7.

[8] Cui YH, Kang JH, Suh Y, Zhao Y, Yi JM, Bae IH, *et al*. Loss of FBXL14 promotes mesenchymal shift and radioresistance of non-small cell lung cancer by TWIST1 stabilization. Signal Transduction and Targeted Therapy. 2021; 6: 272. https://doi.org/10.1038/s41392-021-00599-z.

[9] Xu T, Yin F, Shi K. TMEM158 functions as an oncogene and promotes lung adenocarcinoma progression through the PI3K/AKT pathway via interaction with TWIST1. Experimental Cell Research. 2024; 437: 114010. https://doi.org/10.1016/j.yexcr.2024.114010.

[10] Qin H, Ni H, Liu Y, Yuan Y, Xi T, Li X, *et al*. RNA-binding proteins in tumor progression. Journal of Hematology & Oncology. 2020; 13: 90. https://doi.org/10.1186/s13045-020-00927-w.

[11] Kang D, Lee Y, Lee JS. RNA-Binding Proteins in Cancer: Functional and Therapeutic Perspectives. Cancers. 2020; 12: 2699. https://doi.org/10.3390/cancers12092699.

[12] Wang X, Li J, Zhang C, Guan X, Li X, Jia W, *et al*. Old players and new insights: unraveling the role of RNA-binding proteins in brain tumors. Theranostics. 2025; 15: 5238–5257. https://doi.org/10.7150/thno.113312.

[13] Dassi E. Handshakes and Fights: The Regulatory Interplay of RNA-Binding Proteins. Frontiers in Molecular Biosciences. 2017; 4: 67. https://doi.org/10.3389/fmolb.2017.00067.

[14] Glisovic T, Bachorik JL, Yong J, Dreyfuss G. RNA-binding proteins and post-transcriptional gene regulation. FEBS Letters. 2008; 582: 1977–1986. https://doi.org/10.1016/j.febslet.2008.03.004.

[15] Gerlach K, Zörnig M. FUBP1 (far upstream element (FUSE) binding protein 1). Atlas of Genetics and Cytogenetics in Oncology and Haematology. 2013; 17: 816–820.

[16] Debaize L, Troadec MB. The master regulator FUBP1: its emerging role in normal cell function and malignant development. Cellular and Molecular Life Sciences: CMLS. 2019; 76: 259–281. https://doi.org/10.1007/s00018-018-2933-6.

[17] Wang X, Xing L, Yang R, Chen H, Wang M, Jiang R, *et al*. The circACTN4 interacts with FUBP1 to promote tumorigenesis and progression of breast cancer by regulating the expression of proto-oncogene MYC. Molecular Cancer. 2021; 20: 91. https://doi.org/10.1186/s12943-021-01383-x.

[18] Zheng Y, Dubois W, Benham C, Batchelor E, Levens D. FUBP1 and FUBP2 enforce distinct epigenetic setpoints for MYC expression in primary single murine cells. Commu-

nications Biology. 2020; 3: 545. https://doi.org/10.1038/s42003-020-01264-x.

[19] Zhang F, Xiong Q, Wang M, Cao X, Zhou C. FUBP1 in human cancer: Characteristics, functions, and potential applications. Translational Oncology. 2024; 48: 102066. https://doi.org/10.1016/j.tranon.2024.102066.

[20] Yin H, Gao T, Xie J, Huang Z, Zhang X, Yang F, *et al*. FUBP1 promotes colorectal cancer stemness and metastasis via DVL1-mediated activation of Wnt/β-catenin signaling. Molecular Oncology. 2021; 15: 3490–3512. https://doi.org/10.1002/1878-0261.13064.

[21] Yu J, Peng W, Xue Y, Li Y, Yang L, Geng Y. FUBP1 promotes the proliferation of lung squamous carcinoma cells and regulates tumor immunity through PD-L1. Allergologia et Immunopathologia. 2022; 50: 68–74. https://doi.org/10.15586/aei.v50i5.659.

[22] Gau BH, Chen TM, Shih YHJ, Sun HS. FUBP3 interacts with FGF9 3' microsatellite and positively regulates FGF9 translation. Nucleic Acids Research. 2011; 39: 3582–3593. https://doi.org/10.1093/nar/gkq1295.

[23] Gao Q, Zhou R, Meng Y, Duan R, Wu L, Li R, *et al*. Long noncoding RNA CMPK2 promotes colorectal cancer progression by activating the FUBP3-c-Myc axis. Oncogene. 2020; 39: 3926–3938. https://doi.org/10.1038/s41388-020-1266-8.

[24] Li J, Zhang Z, Guo K, Wu S, Guo C, Zhang X, *et al*. Identification of a key glioblastoma candidate gene, FUBP3, based on weighted gene co-expression network analysis. BMC Neurology. 2022; 22: 139. https://doi.org/10.1186/s12883-022-02661-x.

[25] Wang X, Guo Y, Chen G, Fang E, Wang J, Li Q, *et al*. Therapeutic targeting of FUBP3 phase separation by GATA2-AS1 inhibits malate-aspartate shuttle and neuroblastoma progression via modulating SUZ12 activity. Oncogene. 2023; 42: 2673–2687. https://doi.org/10.1038/s41388-023-02798-0.

[26] Wang HQ, Man QW, Huo FY, Gao X, Lin H, Li SR, *et al*. STAT3 pathway in cancers: Past, present, and future. MedComm. 2022; 3: e124. https://doi.org/10.1002/mco2.124.

[27] Tolomeo M, Cascio A. The Multifaced Role of STAT3 in Cancer and Its Implication for Anticancer Therapy. International Journal of Molecular Sciences. 2021; 22: 603. https://doi.org/10.3390/ijms22020603.

[28] El-Tanani M, Al Khatib AO, Aladwan SM, Abuelhana A, McCarron PA, Tambuwala MM. Importance of STAT3 signalling in cancer, metastasis and therapeutic interventions. Cellular Signalling. 2022; 92: 110275. https://doi.org/10.1016/j.cellsig.2022.110275.

[29] Hu Y, Dong Z, Liu K. Unraveling the complexity of STAT3 in cancer: molecular understanding and drug discovery. Journal of Experimental & Clinical Cancer Research: CR. 2024; 43: 23. https://doi.org/10.1186/s13046-024-02949-5.

[30] Frump AL, Machado RF. Bound Together: RNA Binding Protein Quaking, STAT3, and Pulmonary Vascular Remodeling. American Journal of Respiratory Cell and Molecular Biology. 2023; 69: 119–120. https://doi.org/10.1165/rcmb.2023-0145ED.

[31] Nishinakamura H, Minoda Y, Saeki K, Koga K, Takaesu G, Onodera M, *et al*. An RNA-binding protein alphaCP-1 is involved in the STAT3-mediated suppression of NF-kappaB transcriptional activity. International Immunology. 2007; 19: 609–619. https://doi.org/10.1093/intimm/dxm026.

[32] Zhang L, Zhang Y, Shen D, Chen Y, Feng J, Wang X, *et al*. RNA Binding Motif Protein 3 Promotes Cell Metastasis and Epithelial-Mesenchymal Transition Through STAT3 Signaling Pathway in Hepatocellular Carcinoma. Journal of Hepatocellular Carcinoma. 2022; 9: 405–422. https://doi.org/10.2147/JHC.S351886.

[33] Ohbayashi N, Taira N, Kawakami S, Togi S, Sato N, Ikeda O, *et al*. An RNA biding protein, Y14 interacts with and modulates STAT3 activation. Biochemical and Biophysical Research Communications. 2008; 372: 475–479. https://doi.org/10.1016/j.bbrc.2008.05.073.

[34] Sharma M, Anandram S, Ross C, Srivastava S. FUBP3 regulates chronic myeloid leukaemia progression through PRC2 complex regulated PAK1-ERK signalling. Journal of Cellular and Molecular Medicine. 2023; 27: 15–29. https://doi.org/10.1111/jcmm.17584.

[35] Pastushenko I, Blanpain C. EMT Transition States during Tumor Progression and Metastasis. Trends in Cell Biology. 2019; 29: 212–226. https://doi.org/10.1016/j.tcb.2018.12.001.

[36] Heerboth S, Housman G, Leary M, Longacre M, Byler S, Lapinska K, *et al*. EMT and tumor metastasis. Clinical and Translational Medicine. 2015; 4: 6. https://doi.org/10.1186/s40169-015-0048-3.

[37] Ye X, Brabletz T, Kang Y, Longmore GD, Nieto MA, Stanger BZ, *et al*. Upholding a role for EMT in breast cancer metastasis. Nature. 2017; 547: E1–E3. https://doi.org/10.1038/nature22816.

[38] Nam EH, Lee Y, Moon B, Lee JW, Kim S. Twist1 and AP-1 cooperatively upregulate integrin α5 expression to induce invasion and the epithelial-mesenchymal transition. Carcinogenesis. 2015; 36: 327–337. https://doi.org/10.1093/carcin/bgv005.

[39] Ansieau S, Morel AP, Hinkal G, Bastid J, Puisieux A. TWISTing an embryonic transcription factor into an oncoprotein. Oncogene. 2010; 29: 3173–3184. https://doi.org/10.1038/onc.2010.92.

[40] Cheng GZ, Zhang WZ, Sun M, Wang Q, Coppola D, Mansour M, *et al*. Twist is transcriptionally induced by activation of STAT3 and mediates STAT3 oncogenic function. The Journal of Biological Chemistry. 2008; 283: 14665–14673. https://doi.org/10.1074/jbc.M707429200.

[41] Cho KH, Jeong KJ, Shin SC, Kang J, Park CG, Lee HY. STAT3 mediates TGF-β1-induced TWIST1 expression and prostate cancer invasion. Cancer Letters. 2013; 336: 167–173. https://doi.org/10.1016/j.canlet.2013.04.024.

[42] Zhao D, Besser AH, Wander SA, Sun J, Zhou W, Wang B, *et al*. Cytoplasmic p27 promotes epithelial-mesenchymal transition and tumor metastasis via STAT3-mediated Twist1 upregulation. Oncogene. 2015; 34: 5447–5459. https://doi.org/10.1038/onc.2014.473.

[43] Kim MS, Lee HS, Kim YJ, Lee DY, Kang SG, Jin W. MEST induces Twist-1-mediated EMT through STAT3 activation in breast cancers. Cell Death and Differentiation. 2019; 26: 2594–2606. https://doi.org/10.1038/s41418-019-0322-9.

[44] Jianwei Z, Qi L, Quanquan X, Tianen W, Qingwei W. TMPRSS4 Upregulates TWIST1 Expression through STAT3 Activation to Induce Prostate Cancer Cell Migration. Pathology Oncology Research: POR. 2018; 24: 251–257. https://doi.org/10.1007/s12253-017-0237-z.

[45] Lee KW, Yeo SY, Sung CO, Kim SH. Twist1 is a key regulator of cancer-associated fibroblasts. Cancer Research. 2015; 75: 73–85. https://doi.org/10.1158/0008-5472.CAN-14-0350.

[46] Uthaya Kumar DB, Chen CL, Liu JC, Feldman DE, Sher LS, French S, *et al*. TLR4 Signaling via NANOG Cooperates With STAT3 to Activate Twist1 and Promote Formation of Tumor-Initiating Stem-Like Cells in Livers of Mice. Gastroenterology. 2016; 150: 707–719. https://doi.org/10.1053/j.gastro.2015.11.002.